

PTEN Controls Junction Lengthening and Stability during Cell Rearrangement in Epithelial Tissue

Pierre-Luc Bardet,^{1,3} Boris Guirao,^{1,3} Camille Paoletti,^{1,4} Fanny Serman,¹ Valentine Léopold,¹ Floris Bosveld,¹ Yûki Goya,¹ Vincent Mirouse,² François Graner,^{1,5} and Yohanns Bellaïche^{1,*}

¹Polarity Division and Morphogenesis Team, Institut Curie, CNRS UMR 3215, INSERM U934, 26 rue d'Ulm, 75248 Paris Cedex 05, France
²GReD, CNRS UMR 6293, INSERM U1103, Clermont Université 28, Place Henri Dunant, 63000 Clermont-Ferrand, France

³These authors contributed equally to this work

⁴Present address: Institut de Biologie Moléculaire et Cellulaire, 1 rue Laurent Fries, 67400 Illkirch Cedex, France

⁵Present address: Matière et Systèmes Complexes, CNRS UMR 7057, Université Paris Diderot, 10 rue Alice Domon et Léonie Duquet, 75205 Paris Cedex 13, France

*Correspondence: yohanns.bellaiche@curie.fr
<http://dx.doi.org/10.1016/j.devcel.2013.04.020>

SUMMARY

Planar cell rearrangements control epithelial tissue morphogenesis and cellular pattern formation. They lead to the formation of new junctions whose length and stability determine the cellular pattern of tissues. Here, we show that during *Drosophila* wing development the loss of the tumor suppressor PTEN disrupts cell rearrangements by preventing the lengthening of newly formed junctions that become unstable and keep on rearranging. We demonstrate that the failure to lengthen and to stabilize is caused by the lack of a decrease of Myosin II and Rho-kinase concentration at the newly formed junctions. This defect results in a heterogeneous cortical contractility at cell junctions that disrupts regular hexagonal pattern formation. By identifying PTEN as a specific regulator of junction lengthening and stability, our results uncover how a homogenous distribution of cortical contractility along the cell cortex is restored during cell rearrangement to control the formation of epithelial cellular pattern.

INTRODUCTION

Planar cell rearrangements play a fundamental role in epithelial tissue morphogenesis as they allow the remodeling of tissues while maintaining their cohesiveness. They occur by E-cadherin (E-Cad) adherens junction (AJ) remodeling: cell junctions shorten, bringing four or more cells in contact; after neighbor exchange, new junctions regrow, roughly orthogonal to the previous ones (Keller, 2006). Cell rearrangement thus locally affects cell shape and topology and has been recognized as a major epithelial remodeling process both in invertebrate and vertebrates (Keller, 2006). So far, most studies have focused on the mechanisms of junction shortening that have been extensively studied during the gastrulation of the *Drosophila* embryo (for review, see Lecuit et al., 2011). They rely on the local increase of cortical contractility associated with the dynamic accumula-

tion of myosin II (MyoII) at shortening junctions (Bertet et al., 2004; Nishimura et al., 2012; Rauzi et al., 2010; de Matos Simões et al., 2010; Zallen and Wieschaus, 2004). However, little is known about the mechanisms controlling the lengthening and the stabilization of newly formed junctions in developing tissues.

The length and the stability of junctions are critical to the spatial organization of cells in the epithelium (cell packing, McKenzie et al., 2004; Narimatsu et al., 2009; Nowak et al., 2009; Togashi et al., 2011). Numerous tissues are mostly composed of regular hexagonal cells characterized by AJs of similar lengths (Classen et al., 2005; Gibson et al., 2006; Narimatsu et al., 2009; Tardieu, 1988). At steady state, junction lengths are proposed to be dependent on E-Cad-mediated adhesion, which expands cell-cell contacts, and on MyoII-dependent cortical contractility, which reduces cell junction and perimeters (Lecuit and Lenne, 2007; Maître et al., 2012). Accordingly, quantitative models have analyzed how the adhesion/contractility balance determines junction length, junction tension, and epithelial cell packing (Aigouy et al., 2010; Farhadifar et al., 2007; Graner and Sawada, 1993; Hilgenfeldt et al., 2008; Käfer et al., 2007; Rauzi et al., 2008; Staple et al., 2010). In such models, the regular hexagonal packing corresponds to an energy minimum when all cells have the same physical properties and a homogenous distribution of adhesiveness and contractility on their junctions (Farhadifar et al., 2007; Staple et al., 2010). Although the small GTPase Rap1 is a regulator of E-Cad homogenous distribution in *Drosophila* epithelial cells (Knox and Brown, 2002), the mechanisms promoting a homogenous cortical distribution of MyoII at cell junctions are so far not characterized.

During *Drosophila* pupal wing development, cell rearrangements are concomitant to tissue elongation and hexagonal packing formation (Aigouy et al., 2010). The contraction of the proximal wing hinge region triggers wing blade elongation and oriented cell rearrangements resulting in a tissue with an elongated shape and regular cell packing at the end of morphogenesis, reminiscent of a honeycomb (Aigouy et al., 2010; Classen et al., 2005). This honeycomb-like pattern formation depends on the activity of the Fat/Dachsous and Frizzled planar cell polarity pathways, both of which regulate cell rearrangements (Aigouy et al., 2010; Bosveld et al., 2012; Classen et al., 2005; Harumoto et al., 2010; Ma et al., 2008; Warrington et al., 2013). We

therefore explored whether genes whose loss of function disrupts the final honeycomb packing might be involved in de novo junction formation or elongation during cell rearrangement. Because in vitro studies have shown that formation of new junctions is associated with the activation of the phosphatidylinositol-4,5-bisphosphate 3-kinase (PI3K), whose role in this process remains poorly understood (see discussion in Yamada and Nelson, 2007), we analyzed whether the phosphatidylinositol cycle enzymes control the wing hexagonal cell packing.

Here we characterized how the tumor suppressor PTEN (phosphatase and tensin homolog on chromosome 10) regulates cell packing in the wing. PTEN is frequently inactivated in a wide range of human sporadic tumors (for review, see Chalhoub and Baker, 2009). PTEN is a lipid phosphatase, and its major function is to dephosphorylate phosphatidylinositol (3,4,5)-triphosphate (PIP3) to produce phosphatidylinositol (4,5)-bisphosphate (PIP2). This influences the membrane localization and activation of several key proteins involved in growth control (Chalhoub and Baker, 2009). In epithelia, PTEN participates in cell polarization in conjunction with the Par complex proteins (Martin-Belmonte et al., 2007; Pickering et al., 2013; Pinal et al., 2006), and in cell packing by yet uncharacterized mechanisms (Ma et al., 2008). By combining real-time imaging in *Drosophila* wing epithelium with physical modeling and numerical simulations, we identified PTEN as an essential regulator of junction mechanical properties, which in turn control their lengthening and stability during cell rearrangements. Furthermore our work uncovers an unexpected connection between junction elongation and restoration of a homogenous cortical tensile stress distribution at cell junction, thereby controlling the final epithelial cell packing.

RESULTS

PTEN Loss of Function Gives Rise to Cobblestone and Rosette Packing Characterized by an Excess of Short Junctions

From 28–30 hr after pupa formation (hAPF) onward, *Drosophila* wing intervein epithelium exhibits regular hexagonal cell packing with 75% of cells being six-sided (Classen et al., 2005 and this study) (Figures 1A–1D). Knocking down the phosphatidylinositol cycle enzymes genes (P-L.B., V.L., F.G., and Y.B., unpublished data), we observed that, as previously reported (Ma et al., 2008), the loss of PIP3 phosphatase PTEN function disrupts intervein epithelium cell packing (Figures 1A and 1B). We found that in *pten* tissue, only 50% of the cells were six-sided (Figures 1C and 1D). Furthermore, the tissue exhibits cell patterns with distinctive local cobblestone patterns and some rosette patterns (Figure 1B). The *pten* packing is characterized by a mixing of short and long cell junctions (Figure 1E) that can be quantified by the distribution of junction lengths in the tissue and by the mean heterogeneity of junction lengths for each cell. In the wild-type (WT) tissue, most cell shapes were close to regular hexagons (“honeycomb-like”) and their side length distribution exhibited a single peak (Figure 1F). Instead, *pten* side length distribution was bimodal, with an excess of short sides ($p < 10^{-10}$) (Figures 1E and 1F). Moreover, side length heterogeneity was significantly higher in *pten* cells than in WT cells ($p < 10^{-10}$) (Figures 1G and 1H). Comparable distributions were observed with two *pten* null alleles or in cells expressing a *pten* dsRNA

(*pten*^{RNAi}) (Figures 1F and 1H). PTEN antagonizes the activity of PI3K (Chalhoub and Baker, 2009). Accordingly, overexpression of the PI3K catalytic subunit recapitulated the *pten* phenotype (Figures S1A and S1B available online).

Known deleterious effects of PTEN loss of function in *Drosophila* epithelial tissue including overgrowth and apical-basal polarization defects depend on Akt function (Pinal et al., 2006; Stocker et al., 2002). Our following findings exclude that the *pten* packing phenotype is a consequence of a role of PTEN in cell growth: (1) loss of *akt* function, which rescues the *pten* overgrowth phenotype (Stocker et al., 2002), does not rescue the *pten* packing phenotype (Figures S1C–S1G), (2) the apical area of *pten* cells is identical to the one of wild-type cells between 20 and 30 hAPF (Figures S1H–S1K'), and (3) whereas the overexpression of *rheb* produces a wing overgrowth phenotype similar to the one observed upon PTEN loss of function, the overexpression of *rheb* does not affect hexagonal cell packing (Figures S1L–S1Q). Furthermore the *pten* phenotype is not a consequence of a loss of apical-basal polarization: although some polarity protein levels were slightly more elevated in *pten* tissue, neither apical markers (E-cad, Crumbs, Par3/Bazooka) nor basal ones (Fascin III, Discs-large) were shifted along the apical-basal axis (Figures S1R–S1W'). Accordingly, Par3/Bazooka, a regulator of PTEN localization, does not control cell packing and its loss of function does not suppress the *pten* phenotype (Figures S1X–S1Z). Together, our results suggest the existence of an additional mechanism of action of PTEN in epithelial tissue organization.

Heterogeneous Distribution of Junction Tension Can Account for Local Cobblestone Patterns Observed in *pten* Tissue

Theoretical models have analyzed how the adhesion/contractility balance determines epithelial cell packing (Aigouy et al., 2010; Farhadifar et al., 2007; Graner and Sawada, 1993; Hilgenfeldt et al., 2008; Käfer et al., 2007; Maître et al., 2012; Rauzi et al., 2008). We therefore explored whether and how the modulation of the adhesion/contractility balance at each junction can generate the cell junction length heterogeneity observed in *pten* tissue. To this end, we developed an analytical cell shape model where the adhesion/contractility balance at each side is modeled by the dimensionless “side parameter” λ (see the Supplemental Experimental Procedures). Lambda increases with adhesion and decreases with contractility, and can either be the same at all sides (homogenous), or vary from side to side (heterogeneous).

Considering a periodic cellular lattice to keep the model analytically tractable (Figure 2A, inset), each normalized side tension γ then depends on its side parameter and on the cell normalized perimeter (p): $\gamma = p - \lambda$. First, we determined that when all sides have the same side parameter value and contractility dominates adhesion ($\lambda = \lambda_0$ with $0 < \lambda_0 < p_H$, where $p_H \approx 3.72$ is the normalized perimeter of the regular hexagon), the lattice adopts a honeycomb organization comparable to WT tissue (Aigouy et al., 2010; Farhadifar et al., 2007), with p reaching its minimal value p_H (Hales, 2001), homogenous side length l and tension $\gamma > 0$ (Figures 2A and S2A). Then, we found two mutually exclusive hypotheses both leading to cobblestone patterns, namely hexagons with two sides much shorter than the others,

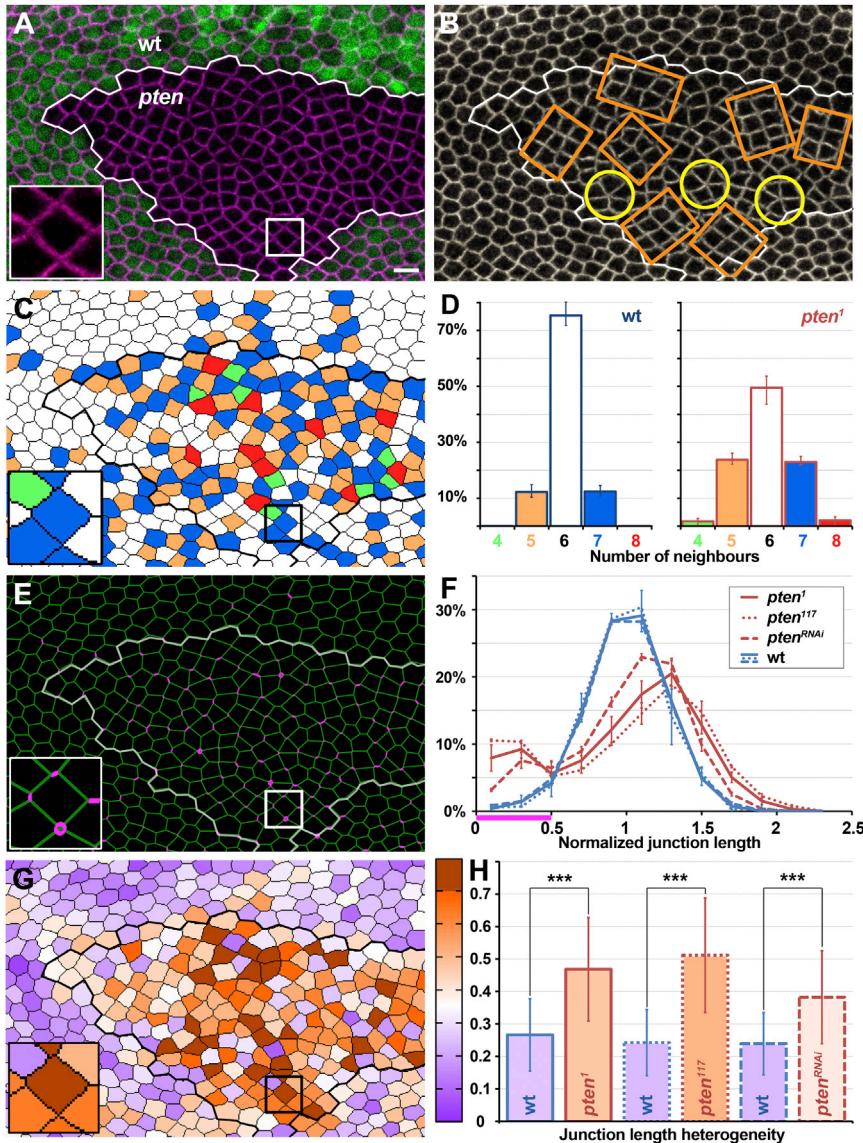


Figure 1. Loss of *pten* Leads to Cell Junction Length Heterogeneity at 30 hAPF

(A–C) A clone of *pten*¹ cells marked by the absence of GFP (green in A; clone boundary is depicted by a white line in A and B) in an otherwise control pupal wing intervein tissue. E-cad staining outlines cell apical junctions (magenta in A; gray in B), and was skeletonized to obtain (C, clone boundary is depicted by a black line). In (B) some cobblestone (orange frames) and rosette patterns (yellow circles) are highlighted. A typical cell within a cobblestone pattern (frame in A and C) is enlarged in inset in (A) and (C). Number of neighbors of each cell is represented by a color in C (4, green; 5, orange; 6, white; 7, blue and 8, red).

(D) Histogram of the number of cell neighbors in WT (left) and *pten*¹ (right) tissue. Bars indicate the SD of distributions.

(E) The tissue region shown in (A) was skeletonized to obtain (E). The *pten* clone boundary is depicted by a white line. Short sides (<0.5 × average length) are shown in magenta and with magenta circles indicating a cobblestone pattern (frame) is enlarged in inset in (E).

(F) Histogram of the junction length distributions in *pten*¹, *pten*¹¹⁷, and *pten*^{RNAi} and their corresponding WT controls. Junction lengths are normalized by the average length. Bars indicate the SD of distributions.

(G) The tissue region shown in (A) was skeletonized to obtain (G). The *pten* clone boundary is depicted by a black line. The junction length heterogeneity per cell is represented by colors, ranging from dark purple (homogeneous, close to 0) to dark orange (very heterogeneous, close to 1). A typical cell within a cobblestone pattern (frame) is enlarged in inset in (G).

(H) Graph of junction length heterogeneity average in *pten*¹, *pten*¹¹⁷, and *pten*^{RNAi} and their corresponding WT control tissues. Colored bars indicate the SD of distributions and stars indicate statistical significance (***) $p < 10^{-10}$.

Quantifications for (D), (F), and (H) were performed on: *pten*¹: eight clones in three wings, 1,736 cells, 4,329 sides; WT control: 2,654 cells, 6,955 sides;

*pten*¹¹⁷: two clones in two wings, 665 cells, 1,829 sides. WT: 509 cells, 1,325 sides; *pten*^{RNAi}: two wings (posterior compartment), 3,291 cells, 9,228 sides; WT: same wings (anterior compartment), 1,262 cells, 3,460 sides. Scale bar represents 5 μm. See also Figure S1.

as observed in parts of *pten* wings (Figure 2B). (1) The “homogeneous and $\gamma = 0$ ” hypothesis (case 1 in Figures 2, S2B, and S2C): all sides have the same side parameter value and adhesion dominates contractility ($\lambda = \lambda_o$ and $\lambda_o > \rho_H$); these cobblestone patterns are characterized by vanishing side tensions ($\gamma = 0$). (2) The “heterogeneous and $\gamma > 0$ ” hypothesis (case 2 in Figures 2B and S2C): cell sides have heterogeneous adhesive/cortical properties, i.e., different λ values; in the model, these cobblestone patterns are characterized by strictly positive side tensions ($\gamma > 0$) that decrease with increasing side length l (Supplemental Experimental Procedures).

To test which of these two hypotheses best describes the *pten* tissue, we probed junction tension γ by measuring the initial relaxation velocity V^o of vertices after laser ablation of single-cell junctions (Figure 2C) (Farhadifar et al., 2007; Hutson et al.,

2009; Rauzi et al., 2008). The mean side tension γ was strictly positive and was similar in WT and *pten* cells (Figure 2D). This rules out that the *pten* phenotype is described by the “homogeneous and $\gamma = 0$ ” hypothesis, but supports the “heterogeneous and $\gamma > 0$ ” hypothesis. Moreover, side tensions γ decreased with side lengths l (Figure 2D); correlations and linear fits of experimental data of γ versus l were similar in WT and *pten* cells, suggesting that the length-tension relationship is unchanged by PTEN loss of function.

Fitting our model to laser ablation data allowed us to estimate the side parameter mean values as well as their ranges of variation: for the WT, we determined a single value, $\lambda_o \approx 2.3 \pm 0.4$ (Figure S2D); and for *pten*, two values $\lambda_S \approx 1.8 \pm 0.4$, $\lambda_L \approx 2.9 \pm 0.4$ (Figure S2E). The study of the λ -diagram for $0 < \lambda < \rho_H$ shows that it is made of two complementary

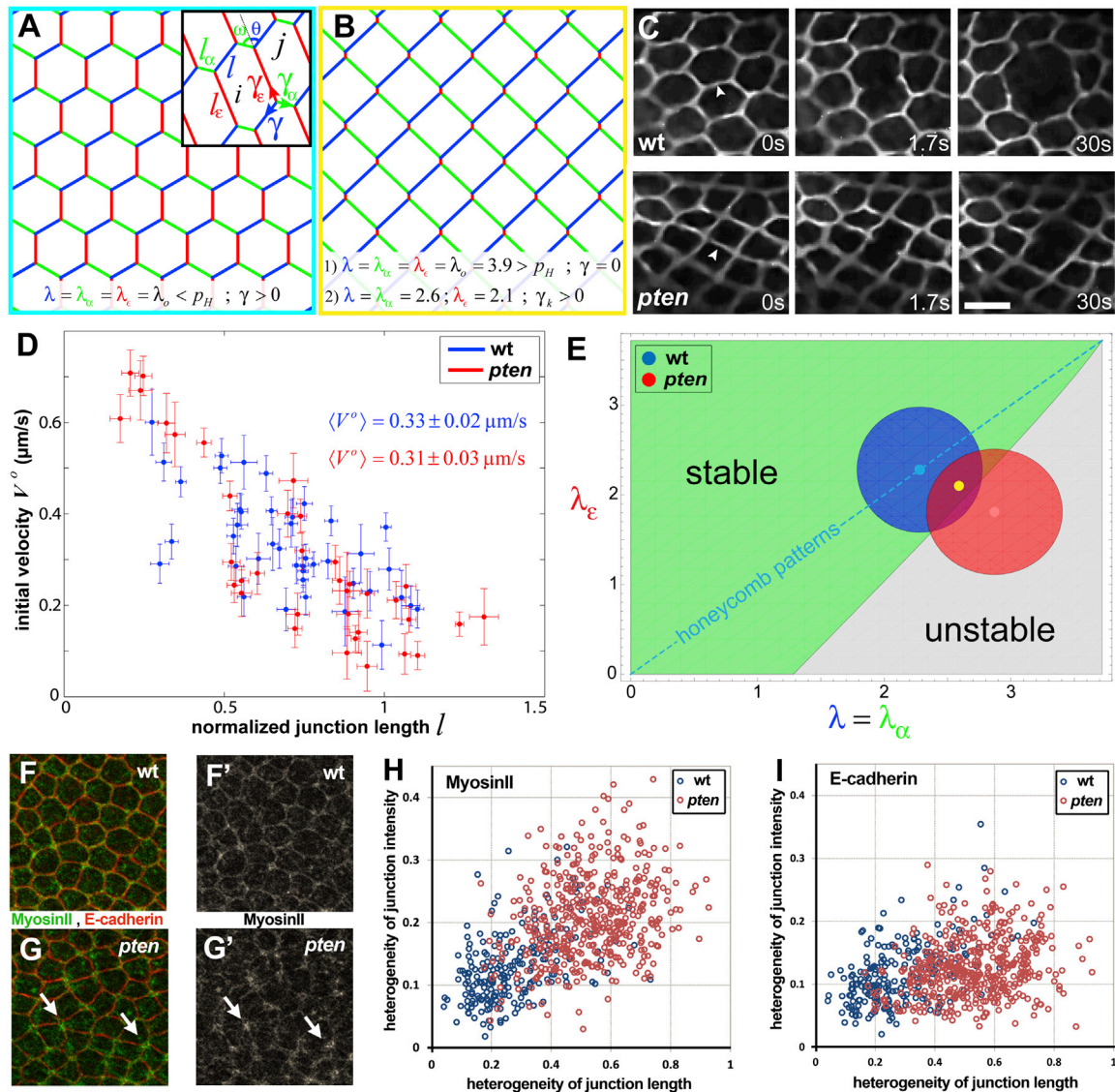


Figure 2. Heterogeneity in Junction Tension Due to Alteration of Adhesion/Contractility Balance Can Account for *pten* Packing

(A) Honeycomb pattern obtained in homogeneous case at any low side parameter value ($\lambda_0 < p_H \approx 3.72$). Inset: model notations and cellular lattice. The lattice is made of identical six-sided cells of constant area A_0 tiling the plane. Force balance is satisfied at each vertex. A network configuration is fully determined by specification of angles (ω, θ) and dimensionless side lengths (l, l_α, l_ϵ). Side length symmetry is broken when these lengths differ.

(B) Cobblestone pattern obtained in either: the “homogeneous and $\gamma = 0$ ” case at high side parameter value ($\lambda_0 = 3.9 > p_H$) or: the “heterogeneous and $\gamma > 0$ ” case with one side having a side parameter (red, $\lambda_\epsilon = 2.1$) lower than the other two (green and blue, $\lambda = \lambda_\alpha = 2.6$).

(C) Vertices right before, 1.7 s and 30 s after laser ablation of a single junction (arrowhead) in WT (top) and *pten*¹ cells (bottom).

(D) Junction tension variation with junction length. Initial velocity after ablation V^0 ($\mu\text{m/s}$) is plotted versus dimensionless side length $l = L / \langle A \rangle^{1/2}$, $\langle A \rangle$ being the mean area of intervein cells. Each point corresponds to a cell junction ablation: blue, WT ($n = 42$); red, *pten*¹ ($n = 36$). Bars indicate measurement errors on junction length and initial velocity.

(E) Diagram of side parameters in the plane $\lambda = \lambda_\alpha$ for λ in $[0, p_H]$. The stable domain is colored in green, the unstable one in gray. Domains representing side parameter ranges obtained from laser ablation experiments [$\langle \lambda_k \rangle - 2\sigma_k; \langle \lambda_k \rangle + 2\sigma_k$] for WT (blue) and *pten* (red) tissues. The cyan and yellow points correspond to averages of WT domain and of stable part of *pten* domain, respectively, and correspond to patterns shown in (A) and (B). The cyan dashed line represents the set of honeycomb patterns.

(F–G’) Confocal images of WT (F and F’) and *pten*^{RNAi} (G and G’) intervein tissue where MyoII is detected by the localization of MyoII-GFP (green in F and G; gray in F’ and G’) and E-Cad (red in F and G). In *pten*^{RNAi} tissue, MyoII-GFP is heterogeneous and accumulates at the short sides (arrows in G and G’). Note that in wild-type and *pten*^{RNAi} tissues, MyoII-GFP can accumulate as circular or star-shape pattern structures around 4-fold vertex, which represent transient accumulation of MyoII:GFP at both the old and newly-formed junctions.

(H and I) Graph of MyoII (H) and E-cad (I) intensity heterogeneity versus cell junction length heterogeneity in WT (blue dots) and in *pten* (red dots) cells.

Scale bar represents 5 μm . See also Figure S2.

domains: a stable one where hexagonal lattices and all three types of sides can exist and be stable (green region in Figure 2E), and an unstable one where hexagonal lattices cannot exist and where the side with highest tension γ disappears before the energy minimum is reached (gray domain in Figure 2E). We next plotted the domains of this λ -diagram that correspond to the ranges of experimental λ values for WT and *pten* tissues found above (Figure 2E). The WT domain lies almost entirely within the stable domain, thereby adopting a stable honeycomb pattern on average. Conversely, the *pten* domain mostly lies in the unstable domain. This implies that, in *pten*, most parameter values found experimentally involve an unstable side, the shortest one, which shrinks and disappears, possibly leading to a new side that can in turn be stable or not. Importantly, the center of the *pten* stable domain (yellow point) corresponds to a cobblestone pattern (Figure 2B), in agreement with experimental observations.

The analysis of laser ablation experiments with our model predicted that: (1) the heterogeneity of cell junction adhesion/contractility balance can account for the local *pten* cobblestone patterns, and (2) the *pten* phenotype involves instability of most short cell junctions. These two predictions prompted us to perform two complementary analyses. First, we aimed at determining whether the junction length heterogeneity observed in *pten* tissue correlates with defects in the distribution of cadherin and/or MyoII along the cell cortex at 28–30 hAPF. Second, we explored during wing development when and how the short junctions are generated and whether they are indeed unstable.

Heterogeneity of Junction Length Is Associated with a Heterogeneous Distribution of MyoII in *pten* Tissue

To determine whether PTEN leads to heterogeneities in adhesion/contractility, we compared the distributions of E-Cad and of the MyoII regulatory light chain (MyoII) (Royou et al., 2004) along the cortex of WT and *pten* cells. In WT tissue at 28–30 hAPF, the distributions of both E-Cad and MyoII are homogenous around the cell cortex in agreement with the fact that the tissue adopts a honeycomb packing (Figures 2F and 2F'). The distribution of E-Cad remained homogeneous in *pten* cells, whereas the MyoII distribution was remarkably heterogeneous along the cell cortex, being strongly increased on short junctions (Figures 2G and 2G'). Moreover, and in contrast to the E-Cad distribution, we found that the increase in heterogeneity of MyoII intensity positively correlated with the increase in junction length heterogeneity (Figures 2H and 2I). Together these results demonstrate that PTEN affects the distribution of MyoII along the cell cortex. They further suggest that the heterogeneity in MyoII-dependent cortex contractility drives the tension heterogeneity found in *pten* mutant cells.

In *Drosophila* embryo, MyoII is proposed to accumulate at junctions in response to MyoII-dependent tension in adjacent junctions (Fernandez-Gonzalez et al., 2009). This raised the possibility that the PTEN loss of function might induce nonautonomous defects in either cell packing or MyoII localization in cells surrounding the *pten* tissue. Yet, small WT tissue islands surrounding by large *pten* tissue showed a regular packing and normal distribution of MyoII (Figures S2F, S2G, and S2J). In addition, small *pten* clones surrounded by wild-type tissue manifested a packing and a MyoII distribution defects (Figures S2H–S2J). Furthermore, the analysis of junction length distribu-

tions at the frontier of WT and *pten* tissues revealed that only the junctions that are common to a *pten* and a WT cell are affected (Figure S2K, purple plain line). Collectively, our results show that loss of PTEN function causes a local defect in cell packing associated with heterogeneous distribution of MyoII localization.

PTEN Loss of Function Causes Cell Rearrangement Defects Where Newly Formed Junctions Fail to Elongate and Become Unstable

In parallel, we imaged a functional E-Cad:GFP (Oda and Tsukita, 2001) in pupal wings expressing a *pten* dsRNA (*pten*^{RNAi}) using the Gal4/Gal80ts system (McGuire et al., 2003) to abrogate PTEN function in the posterior compartment during pupal development. The anterior compartment was used as a WT internal control and its development proceeds in two phases (Aigouy et al., 2010). In a first phase from 20 to 24 hAPF, cells undergo a last round of divisions, rearrange and flow toward the proximal part of the wing. In a second phase from 24 to 30 hAPF, in absence of cell division and flow, cells undergo oriented rearrangements, generating a honeycomb-like packing (Movie S1). In *pten* tissue at 20 hAPF, no major difference with WT tissue was observed, as reflected by the distribution of junction lengths (Figures S3A, S3D, and S3G). From 20 hAPF onward, during and after cell divisions and cell flow, the difference between WT and *pten* tissues became gradually more pronounced leading to the formation of the cobblestone and rosette packing (Figures S3B–S3I; Movie S1). Because cell rearrangement was the only process common to both phases, this prompted us to analyze the dynamics of cell rearrangements in WT and *pten* tissues by tracking individual cell junctions from 23 to 29 hAPF.

In WT and *pten* tissues, the number of junctions that initiated a cell rearrangement was similar (30% in WT, $n = 957$ and 31% in *pten*, $n = 723$). Nevertheless, we observed important differences in junction remodeling during cell rearrangements. In WT tissue, when a cell junction shrank and disappeared through a cell rearrangement, it rarely rearranged back and forth more than two additional times (Figures 3A, 3B, and S3L; Movie S2A). In sharp contrast, in *pten* tissue, when a junction initiated a cell rearrangement, the newly formed junction remained short and very often (85%) shrank shortly thereafter, giving rise to a short unstable junction as it kept on rearranging back and forth several times (Figures 3D, 3E, and S3M; Movie S2B). This demonstrates that PTEN loss of function prevents junction elongation during cell rearrangement and leads to unstable junctions, as predicted by our model and laser ablations.

To further establish whether the *pten* defects in junction remodeling is associated with the formation of short junctions, we categorized in both WT and *pten* tissues the distribution of the final junction length as a function of the number of cell rearrangements they underwent. In the WT tissue, independently of the number of cell rearrangements that a junction underwent, most of the junctions found at 29 hAPF are long junctions, lengths of which are close to the average length (Figure 3C). In *pten* tissue, nonrearranging junctions mainly produce long junctions, which length distribution is similar to the WT ones (dotted light red line in Figure 3F). In contrast, we observed that junctions having rearranged more than four times are the main source of the excess of short junctions observed in the *pten* tissue (dark red line in Figure 3F, 91% of the short junctions).

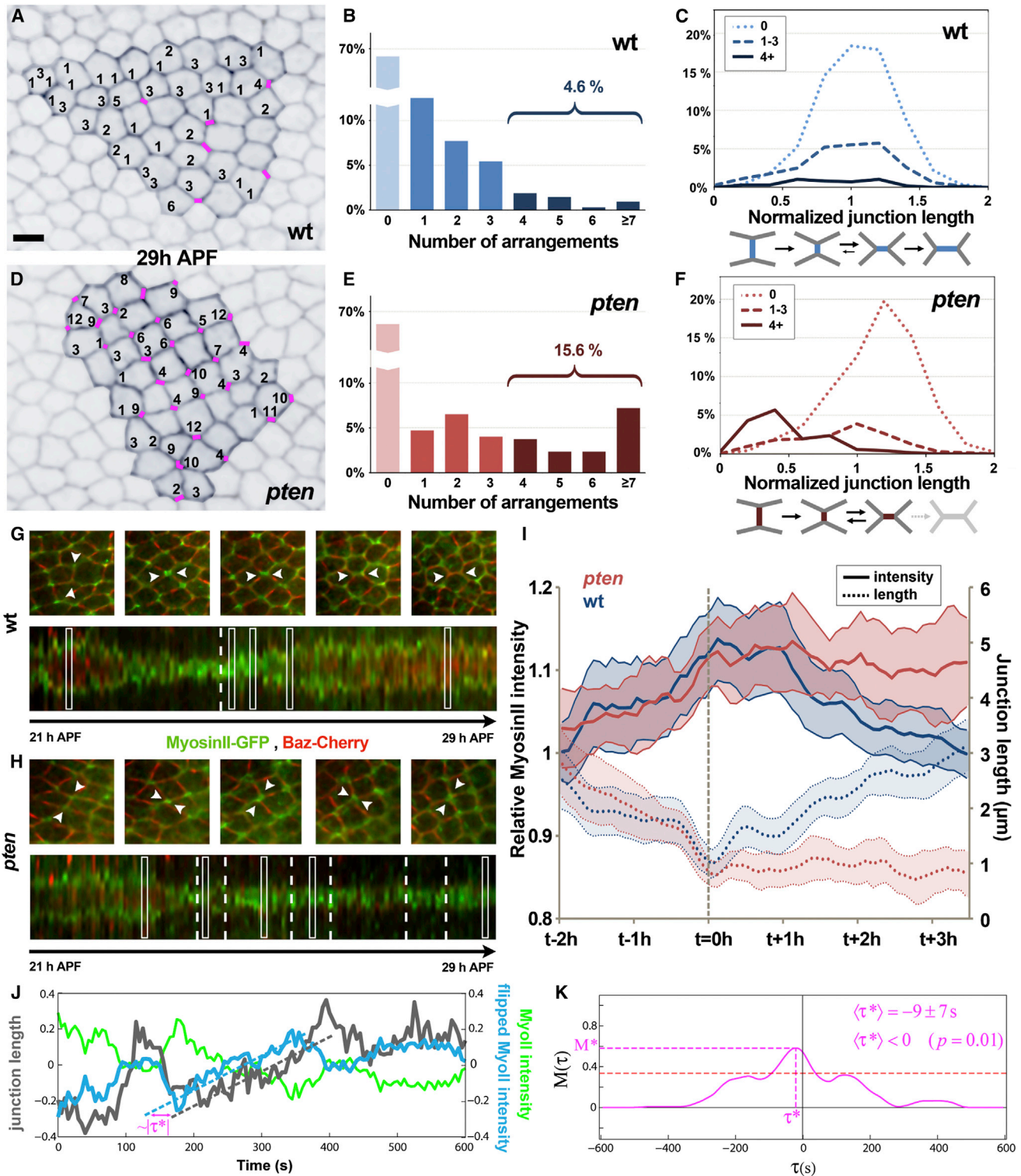


Figure 3. *pten* Cells Undergo Numerous Successive Cell Rearrangements, Giving Rise to Short Junctions Enriched in MyoII that Prevents Their Elongation

(A) Last confocal image of a 6 hr long (23–29 hAPF) E-Cad-GFP time-lapse movie in a WT tissue. 129 WT cell junctions were tracked. Junctions formed by cell rearrangement during the filmed period are labeled with the number of rearrangements they underwent. Short junctions ($<0.5 \times$ average length, $n=6$) are shown in magenta.

(B) Bar plot of cell junctions according to the number of cell rearrangements they underwent in WT tissue. 957 junctions were tracked. Light blue, nonrearranging junctions; blue, junctions undergoing one to three rearrangements; dark blue, junctions undergoing four or more cells rearrangements.

(legend continued on next page)

Taken together, our results demonstrate that the excess of short junctions observed in *pten* tissue is associated with a failure of junction lengthening during cell rearrangement accompanied by junction instability.

MyoII Is Enriched at Newly Formed Junctions during Cell Rearrangements

Our analyses have shown that the loss of PTEN activity is associated with: (1) an increased level of MyoII at short junctions, and (2) a failure of junction lengthening during cell rearrangement leading to the formation of unstable junctions. Because MyoII activity has been so far only linked to junction shortening during cell rearrangements that have been described as irreversible processes (Bertet et al., 2004; Rauzi et al., 2010; de Matos Simões et al., 2010; Zallen and Wieschaus, 2004), current models do not account for these two observations. We therefore explored MyoII dynamics during both junction shortening and lengthening using a functional GFP-tagged MyoII light chain (Royou et al., 2004) (Figures 3G and 3H). In WT wing tissue, MyoII-GFP intensity increased at the cell junction concomitantly to its shortening (Figure 3G). When the rearranging cells formed a 4-fold vertex, MyoII-GFP became strongly concentrated all around this vertex, suggesting that the four cells contributed to this enrichment (Figure 3G). Consistent with this, we detected a strong MyoII-GFP signal at the newly formed junction that faded as the junction lengthened (Figure 3G; Movie S2C). Accordingly, the quantification of MyoII-GFP signal during junction elongation revealed a striking correlation between the decrease of MyoII-GFP concentration and the elongation of the newly formed junction (blue in Figure 3I, $n = 24$). Fast time-lapse imaging of MyoII-GFP dynamics during junction elongation confirmed an inverse correlation between MyoII-GFP level and junction length at short timescale (Figure 3J). Moreover, the analysis of time correlations between MyoII-GFP dynamics and junction length dynamics establishes that the reduction of MyoII-GFP levels at the junction precedes junction elongation by 9 ± 7 s ($n = 7$, $p < 0.01$; Figures 3K and

S3N–S3O'), ruling out that the decrease in MyoII-GFP level is a consequence of junction elongation.

In *pten* tissue, no defects in MyoII-GFP accumulation or junction length were observed during junction shrinkage (Figures 3H, red in 3I, $n = 14$; Movie S2D). However, following the 4-fold vertex stage, MyoII-GFP remained concentrated all along the short junctions, which failed to elongate and kept on rearranging (Figure 3H, red in 3I, $n = 14$; Movie S2D). The results demonstrate that in WT tissue, MyoII is unexpectedly enriched at newly formed junctions and that its concentration decreases during junction elongation in a PTEN-dependent manner.

PIP3 Levels Decrease during Junction Elongation

We then explored the dynamics of PIP3 during cell rearrangements. We observed that the specific PIP3 probe, the PH domain (for Pleckstrin homology) of GRP1 fused to GFP (PH_(PIP3)-GFP) (Britton et al., 2002), accumulates at the newly formed junction and its level decreases as the junction elongates (Figures 4A and 4C). As expected, in *pten* tissue, the overall PIP3 level was increased at the cell membrane relative to the WT tissue (Figure S4A). Moreover, we found that the relative level of PIP3 increased during junction shortening. However, in *pten* tissue PIP3 level failed to significantly decrease at the unstable rearranging junctions that do not regrow (Figures 4B and 4C). These results further argue for a regulatory role of PTEN during junction elongation.

Rok Activity Is Required for the Short Junction Phenotype in *pten* Tissue

MyoII activity is positively and negatively controlled by regulators that therefore modulate cortical tension (Clark et al., 2007). Rho-kinase (Rok) is an essential regulator of MyoII activity (Amano et al., 2010; Winter et al., 2001). We therefore generated a functional Rok-GFP transgene and imaged the dynamics of Rok-GFP during junction remodeling. In WT tissue, Rok-GFP is transiently enriched at newly formed junctions and decreases as junctions lengthen, as observed for MyoII-GFP (Figures 4D and 4F,

(C) Histogram of the distribution of junction lengths categorized according to the number of cell rearrangements they underwent in WT tissue. The color code used is the same as in (B). Below the histogram, a schematic of the typical rearrangement process in a WT tissue is shown.

(D) Last confocal image of 6 hr long (23–29 hAPF) E-Cad-GFP time-lapse movie in a *pten*^{RNAi} tissue. 127 *pten*^{RNAi} cell junctions were tracked. Junctions formed by cell rearrangement during the filmed period are labeled with the number of rearrangements they underwent. Short junctions ($<0.5 \times$ average length, $n = 28$) are shown in magenta.

(E) Bar plot of cell junctions according to the number of cell rearrangements they underwent in *pten*^{RNAi} tissue. 723 junctions were tracked. Light red, non-rearranging junctions; red, junctions undergoing one to three rearrangements; dark red, junctions undergoing four or more cells rearrangements.

(F) Histogram of the distribution of junction lengths categorized according to the number of cell rearrangements they underwent in *pten*^{RNAi} tissues. The color code used is the same as in (E). Below the histogram, a schematic of the typical rearrangement process in *pten*^{RNAi} tissue is shown.

(G and H) Representative images (top panels) and kymographs (bottom panels) of MyoII-GFP (green) and Bazooka-Cherry (Baz-Cherry, red) time-lapse imaging during cell rearrangements in WT (G) and *pten*^{RNAi} (H) tissues. Top panels: the tracked junctions are highlighted by arrowheads. Bottom panels: white rectangular boxes outline the successive temporal positions corresponding to the images shown in the above panels. White dashed bars: timings of 4-fold vertices created by cell rearrangements.

(I) Graph of the average relative intensity of MyoII-GFP (solid lines with SD shown as a shaded region) and of the junction length (dashed lines with the SD shown as shaded region) during cell rearrangements in a WT tissue (blue) and in a *pten*^{RNAi} tissue (red).

(J) Graph of time evolution of relative junction length $L(t)$ (gray) and relative MyoII-GFP intensity $MyoII(t)$ (green) determined by high time-resolution time-lapse video (12 frames min^{-1}). Because MyoII-GFP intensity and junction length are anticorrelated, MyoII-GFP intensity was flipped to $-MyoII(t)$ (blue; see Supplemental Experimental Procedures) to emphasize and measure the time delay between MyoII-GFP and junction length dynamics.

(K) Delay function $M(\tau)$ (that compares $L(t)$ to $MyoII(t+\tau)$; see Supplemental Experimental Procedures; Figure S3) reaches a maximum M^* for the value of the time delay τ minimizing the area between the two curves ($\tau^* = -21$ s for the curves in J). Seven out of eight analyses displayed a correlation between variations of $MyoII$ and L ($M^* > M_{\text{random}} = 0.33$, dashed red line), and yielded a significantly negative average value $\langle \tau^* \rangle = -9 \pm 7$ s ($n = 7$, $p < 0.01$), showing that MyoII intensity variations precede junction length variations.

Scale bar represents 5 μm . See also Figure S3 and Movies S1 and S2.

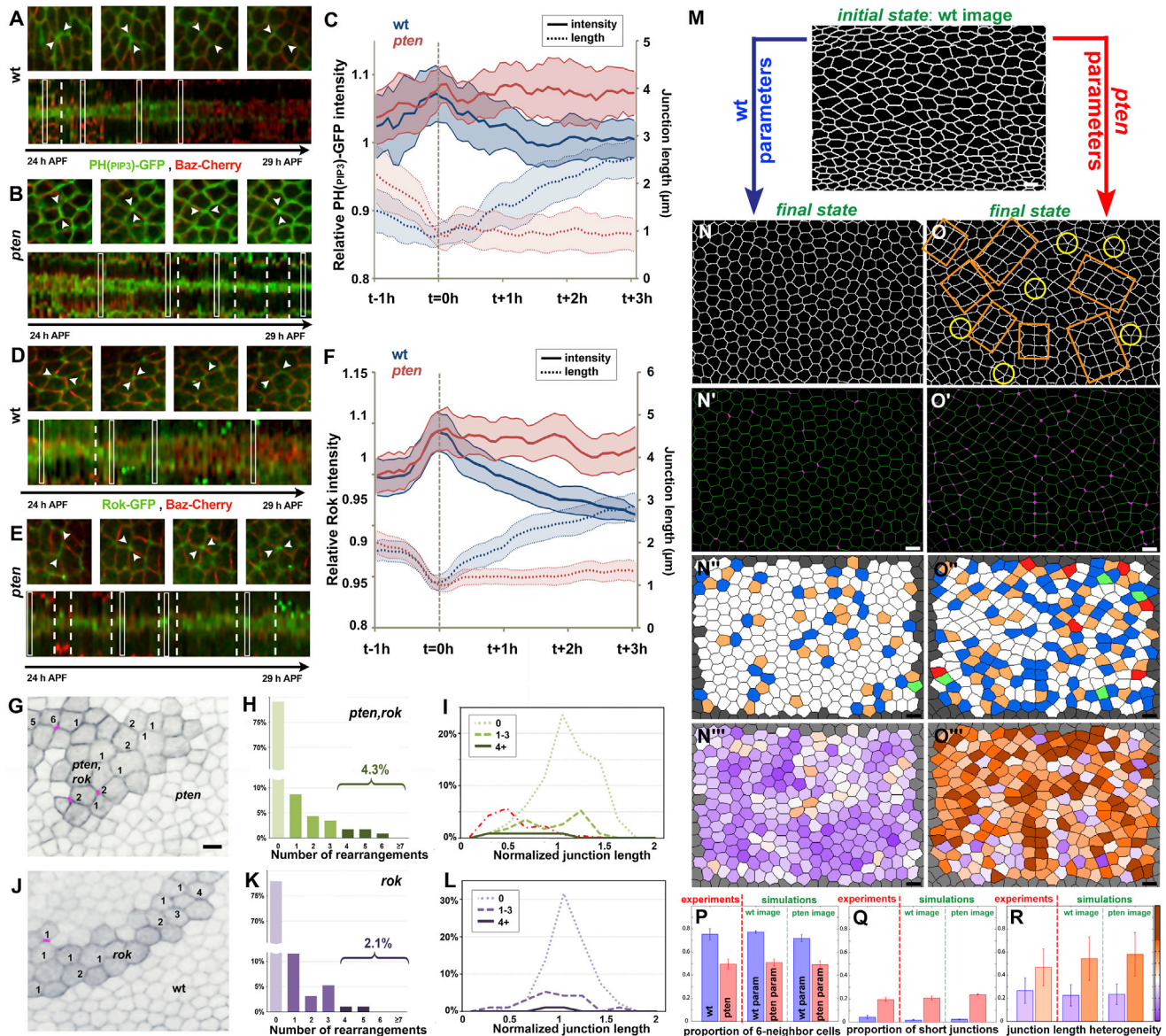


Figure 4. Maintenance of Cortical Tension Accounts for the *pten* Phenotypes

(A and B) Representative images (top panels) and kymographs (bottom panels) of PH(PIP3)-GFP (green) and Baz-Cherry (red) time-lapse imaging during cell rearrangements in WT (A) and *pten*^{RNAi} (B) tissues. Top panels: the tracked junction is highlighted by arrowheads. Bottom panels: white rectangular boxes outline the successive temporal positions corresponding to the images shown in the above panels. White dashed bars: timings of 4-fold vertices created by cell rearrangements.

(C) Graphs of average relative intensity of PH(PIP3)-GFP (solid lines and SD shown as a shaded region) and of junction length (dashed lines and SD shown as shaded region) during cell rearrangement in a WT (blue) and *pten*^{RNAi} (red) tissues.

(D and E) Typical images (top panels) and kymographs (bottom panels) of Rok-GFP (green) and Baz-Cherry (red) time-lapse imaging during cell rearrangements in WT (D) and *pten*^{RNAi} (E) tissue. Top panels: the tracked junction is highlighted by arrowheads. Bottom panels: white rectangular boxes outline the successive temporal positions corresponding to the images shown in the above panels. White dashed bars: timings of 4-fold vertices created by cell rearrangements.

(F) Graph of average relative intensity of Rok-GFP (solid lines with SD shown as a shaded region) and of junction length (dashed lines) during cell rearrangement in WT (blue) and *pten*^{RNAi} (red) tissues.

(G) Last confocal images of a 6 hr long (23–29 hAPF) E-Cad-GFP time-lapse movie of a representative *rok*² clone in a *pten*^{RNAi} tissue. A total of 115 *rok*², *pten*^{RNAi} cell junctions were tracked. Junctions formed by cell rearrangement during the filmed period are labeled with the number of rearrangements they underwent. Short junctions (<0.5 × average length, n = 3) are shown in magenta.

(H) Bar plot of cell junctions according to the number of cell rearrangements they underwent in *pten*^{RNAi}, *rok*² tissue. A total of 115 junctions were tracked. Light green, nonrearranging junctions; green, junctions undergoing one to three rearrangements; dark green, junctions undergoing four or more cells rearrangements. (I) Histogram of the distribution of junction lengths in *pten*^{RNAi}, *rok*² tissue categorized according to the number of rearrangements they underwent. The color code used is the same as in (H). For comparison, the dashed red line (I) represents the distribution of the short and highly rearranging junction lengths in *pten* tissue.

(legend continued on next page)

$n = 27$). Conversely, in *pten* tissue, Rok-GFP intensity remained high at the newly formed junctions that failed to elongate (Figures 4E and 4F, $n = 24$).

Having found that MyoII-GFP level decreases prior to junction elongation, we investigated whether the downregulation of MyoII activity was necessary for junction elongation during cell rearrangement by testing whether a loss of Rok activity could suppress the PTEN loss of function phenotypes. To this end, we generated small *rok* clones in a *pten*^{RNAi} tissue and analyzed both the cell packing and the cell rearrangement dynamics. In such experimental conditions, cytokinesis did not seem to be impaired because cell apical areas were only mildly increased, likely due to a loss of contractility associated with an observed decrease of MyoII cortical localization (Figure S4B). Noticeably, we found that *rok* clones generated in *pten* tissue suppressed the effect of PTEN loss of function on cell packing, namely the excess of short junctions (Figure 4G; purple line in Figure S4C). Despite a slightly higher proportion of nonrearranging junctions (1.15-fold), the rearranging junctions neither produced an excess of short junctions nor fluctuated extensively, but lengthened to produce long cell junctions as observed in the WT tissue (Figures 4H–4I). Furthermore, the packing and cell rearrangement dynamics in double *pten*, *rok* tissue is similar to the one observed in *rok* single mutant tissue (Figures 4J–4L; green line in Figure S4C). This genetic evidence demonstrates that Rok is needed to induce the cell rearrangement and packing defects observed in *pten* tissue. Together with our analysis of MyoII and Rok dynamics during cell rearrangement, our results strongly indicate that PTEN is necessary to downregulate MyoII activity during cell rearrangement.

Altogether our results uncover PTEN as a specific regulator of junction lengthening and stability during cell rearrangement. Furthermore they support a mechanism whereby PTEN regulates the PIP3 levels at newly formed junction to decrease Rok-dependent MyoII contractility, thereby promoting junction lengthening and stabilization.

Maintenance of High Tension in Newly Formed Junctions Accounts for *pten* Cobblestone and Rosette Packing

Having found that PTEN locally regulates cell junction contractility during cell rearrangements, we investigated whether

this local role was sufficient to explain the cobblestone and rosette patterns observed at the global level in *pten* tissue. To this end, we performed computer simulations based on the cellular Potts model that is a general algorithm to simulate groups of cells and to capture the disordered nature of epitheliums (Graner and Glazier, 1992; Krieg et al., 2008). To take into account the proximal-distal elongation of wing cells due to hinge contraction (Aigouy et al., 2010), we started the simulations with a segmented image of an actual WT tissue at 24 hAPF, and we let this tissue evolve to a minimum of energy with the two distinct sets of λ side parameters previously inferred from our laser ablations in WT and *pten* tissues (Figures 2E, S2D, and S2E). In the WT case, each junction was assigned the same λ parameter ($\lambda_o = 2.3$). Alternatively, in the *pten* case, we used two distinct λ parameters ($\lambda_L = 2.9$ and $\lambda_S = 1.8$). Indeed, because our experimental results showed that shorter junctions, including newly formed ones, are under higher tension due to higher level of MyoII (Figures 2D, 2G, 2H, and 3I), we assigned λ_S to the shortest sides ($l \leq 0.5$) and newly formed ones, and λ_L to the longest sides in initial image ($l > 0.5$). Numerical simulations starting from WT segmented images at 24 hAPF and run with WT parameters displayed a relaxation of elongated cell shapes via cell rearrangements and yielded final patterns in very good agreement with the experimental WT honeycomb-like packing at 30 hAPF (Figures 4M and 4N–4N'''; Movie S3A–A'''). In sharp contrast, simulations starting from the same WT images but run with the *pten* parameters displayed many sides that failed to lengthen and to complete cell rearrangements, and yielded final patterns displaying typical cobblestone and rosette patterns, like the ones observed in *pten* tissue (Figures 4M, 4O–4O'''; Movie S3B–S3B'''). The quantitative analysis of these simulated final packings displayed final proportions of six neighbor cells, short junctions, and junction length heterogeneity very similar to those observed in WT and *pten* tissues at 30 hAPF (Figures 4P–4R). Interestingly, the same results were obtained in simulations starting with a segmented image of *pten* tissue at 24 hAPF (Figures 4P–4R and S4D–S4F'''). Taken together, our results show that the local maintenance of high tension in newly formed junctions can account for the global cobblestone and rosette packing characterizing *pten* wings.

(J) Last confocal image of a 6 hr long (23–29 hAPF) E-Cad-GFP time-lapse movie of a representative *rok*² clones in a WT tissue. A total of 95 *rok*² cell junctions were tracked. Junctions formed by cell rearrangement during the filmed period are labeled with the number of rearrangements they underwent. Short junctions ($<0.5 \times$ average length, $n = 1$) are shown in magenta.

(K) Bar plot of cell junctions according to the number of cell rearrangements they underwent in a representative *rok*² clone in a WT tissue. A total of 95 junctions were tracked. Light purple, nonrearranging junctions; purple, junctions undergoing one to three rearrangements; dark purple, junctions undergoing four or more rearrangements.

(L) Histogram of the distribution of junction lengths in *rok*² tissue categorized according to the number of rearrangements they underwent. The color code used is the same as in (K).

(M–O''') Numerical simulations of WT and *pten* tissues. Segmented experimental image of WT tissue at 24 hAPF used as initial state by both simulations using parameters of WT (blue arrow) and *pten* (red arrow) (M). Typical final state of simulations run with WT parameters resulting in honeycomb-like packing (N) and displaying few short junctions (N'), a small disorder in number of neighbors (N''), and a low junction length heterogeneity (N'''). Color codes as in Figure 1. Typical final state of simulations run with *pten* parameters resulting in cobblestone (orange) and rosette (yellow) packing (O), and many short junctions (O'), a large disorder of number of neighbors (O''), and a large junction length heterogeneity (O'''). Color codes as in Figure 1.

(P–R) Comparison of quantitative analyses of cell packings in experimental WT and *pten* tissues at 28–30 hAPF (left in P–R; data from Figures 1D, 1F, and 1H), in simulations run with WT and *pten* parameters starting with segmented images from WT tissue ($n = 3$ simulations) (middle in P–R), and in simulations run with WT and *pten* parameters starting with segmented images from *pten* tissue (right in P–R) ($n = 4$ simulations). Bars indicate the SD of distributions. (P) Proportion of six neighbor cells. (Q) Proportion of normalized junction lengths satisfying $l < 0.5$. (R) Cellular junction length heterogeneity.

Scale bars represent 5 μm . See also Figure S4 and Movie S3.

Defects in Junction Elongation and Hexagonal Packing Are Associated with Defects in Tissue Morphogenesis, Tissue Planar Polarization, and Tissue Architecture

The identification of *pten* as a regulator of both junction dynamics during cell rearrangements and of cell regular hexagonal shapes in the wing gives the opportunity to study the contribution of these processes to tissue morphogenesis, PCP, and organ architecture (ridges of the wing cuticle in this study). We first analyzed the contribution of PTEN to tissue dynamics and morphogenesis between 24 and 29 hAPF, a period over which we have characterized the role of PTEN in junction dynamics, and during which the tissue packing becomes honeycomb-like (Aigouy et al., 2010; Classen et al., 2005). We compared tissue deformation and the underlying cell dynamics in terms of cell rearrangements and cell shape changes in WT and *pten* tissues by applying a quantitative framework that we have developed and validated recently (Figures 5A–5A''; Supplemental Experimental Procedures) (Bosveld et al., 2012). We found that the WT tissue displays important contributions of both AP oriented cell rearrangements and PD oriented cell contraction (Figures 5B and 5C; see also Aigouy et al., 2010). Strikingly, these contributions cancel out, showing that AP cell rearrangements compensate the PD cell contraction, leading to the formation of regular hexagons without significant change in tissue shape ("wt" in Figure 5C and sketch in Figure 5A''). Performing the same analysis on *pten* tissue and subtracting it from the WT analysis enabled us to isolate the defects associated with PTEN loss of function (Bosveld et al., 2012). In agreement with our results on the role of PTEN in junction dynamics and cell packing, PTEN loss of function results in significant defects in both cell rearrangements and cell shape changes. Importantly, these two processes do not cancel out anymore, leading to a defect in tissue contraction along a direction pointing upward the PD axis ("wt-*pten*" in Figure 5C). Accordingly, PTEN loss of function results in adult wings that are slightly more elongated along this direction than the WT ones (Figure 5D). Our analysis of tissue morphogenesis in WT and *pten* wings therefore illustrates that cell rearrangements play a role in coordinating the dynamics of individual cells and the shape of the global tissue.

To test the role of cell rearrangements for the fine-tuning of global PCP alignment along the wing P-D axis (Aigouy et al., 2010), we then determined the intensity, the individual cell planar polarization and the global tissue polarization using Stbm-YFP as a PCP marker (Bellaïche et al., 2004). Although the intensity and the individual cell polarization were similar in WT and *pten* cells, the global tissue PCP relative to the PD axis was significantly affected in absence of *pten* function (Figures 5E–5H). Finally, the regular hexagonal cell packing is proposed to have a key contribution to generate ridges of the adult wing cuticle that are proposed to impact the tissue architecture and mechanics (Doyle et al., 2008). We found that loss of PTEN function drastically affect the ridge organization in the adult wing (Figures 5I and 5J). Collectively, the characterization of the function of PTEN in cell rearrangements establishes the contribution of cell rearrangements to the establishment of the final tissue and cell shapes, PCP global polarization and tissue architecture.

CONCLUSION

Previous studies of junction remodeling established that the dynamics of acto-myosin network generates the cortical contractile forces necessary for junction shortening (Bertet et al., 2004; Rauzi et al., 2008; de Matos Simões et al., 2010; Zallen and Wieschaus, 2004) and implicitly assumed that junction elongation is a passive relaxation process that does not involve any specific regulation (Aigouy et al., 2010; Farhadifar et al., 2007; Glazier and Graner, 1993; Hilgenfeldt et al., 2008; Käfer et al., 2007; Rauzi et al., 2008). Here, we identified PTEN as a specific regulator of junction elongation and stability during cell rearrangement. We observed that the newly formed junction is initially enriched in MyoII and PIP3, which is consistent with the MyoII and PI3K recruitments observed upon E-cad engagement in cell culture models (Papusheva and Heisenberg, 2010). However, in such models, Rok-dependent MyoII contractility is usually proposed to promote junction expansion by pulling on junction edges (Yamada and Nelson, 2007). In an epithelial tissue, our work uncovered that junction lengthening is coupled to the PTEN-dependent decrease of cortical distribution of MyoII that leads to the restoration of an homogeneous cortical contractility around the cortex of cells. This homogenous distribution is required for the formation of a stable, honeycomb-like cell packing as observed in several epithelial tissues (Classen et al., 2005; Farhadifar et al., 2007; Gibson et al., 2006; Narimatsu et al., 2009; Tardieu, 1988). Our findings thus establish that junction elongation is a PTEN-controlled process acting as a critical regulatory step during cell rearrangement. Two nonmutually exclusive models can account for the temporal and spatial regulation of PIP3 level during junction elongation by PTEN. (1) As observed in cell culture upon cell-cell contact formation (Perez et al., 2008; reviewed in Rivard, 2009), PI3K-dependent increase of PIP3 level at the cell-cell contact can be antagonized by a homogenous activity of PTEN at the cell junction, and (2) the activity of PTEN or its recruitment might be regulated locally during junction elongation. Interestingly, the Rok kinase was shown to phosphorylate PTEN and to trigger its activation during cell migration (Li et al., 2005), suggesting a model whereby the initial activation of Rok can initiate a negative feedback loop to promote local activation to PTEN, hence junction elongation and reduction of cortical tension.

Our work also highlights that cellular pattern formation involves reversibility and fluctuations of rearrangements, which could provide the tissue with a mean to explore the energy landscape of cellular patterns. We foresee that mechanisms promoting MyoII homogenous distribution could be more general and drive the restoration of cell contractility symmetry following cell polarization and cell cytokinesis.

EXPERIMENTAL PROCEDURES

Fly Stocks, Genetics, and Molecular Biology

The stocks used were obtained from the Bloomington Stock Center and raised at 25°C, unless otherwise mentioned. All stocks and associated references are described in the Supplemental Experimental Procedures. Loss of function clones were generated using the hs-FLP/FRT system (Xu and Rubin, 1993). Typically, heat shocks of 15 min (for *pten* mutant clones) or 1 hr were carried out 3 days before pupa formation (BPF). White pupae were picked and timed

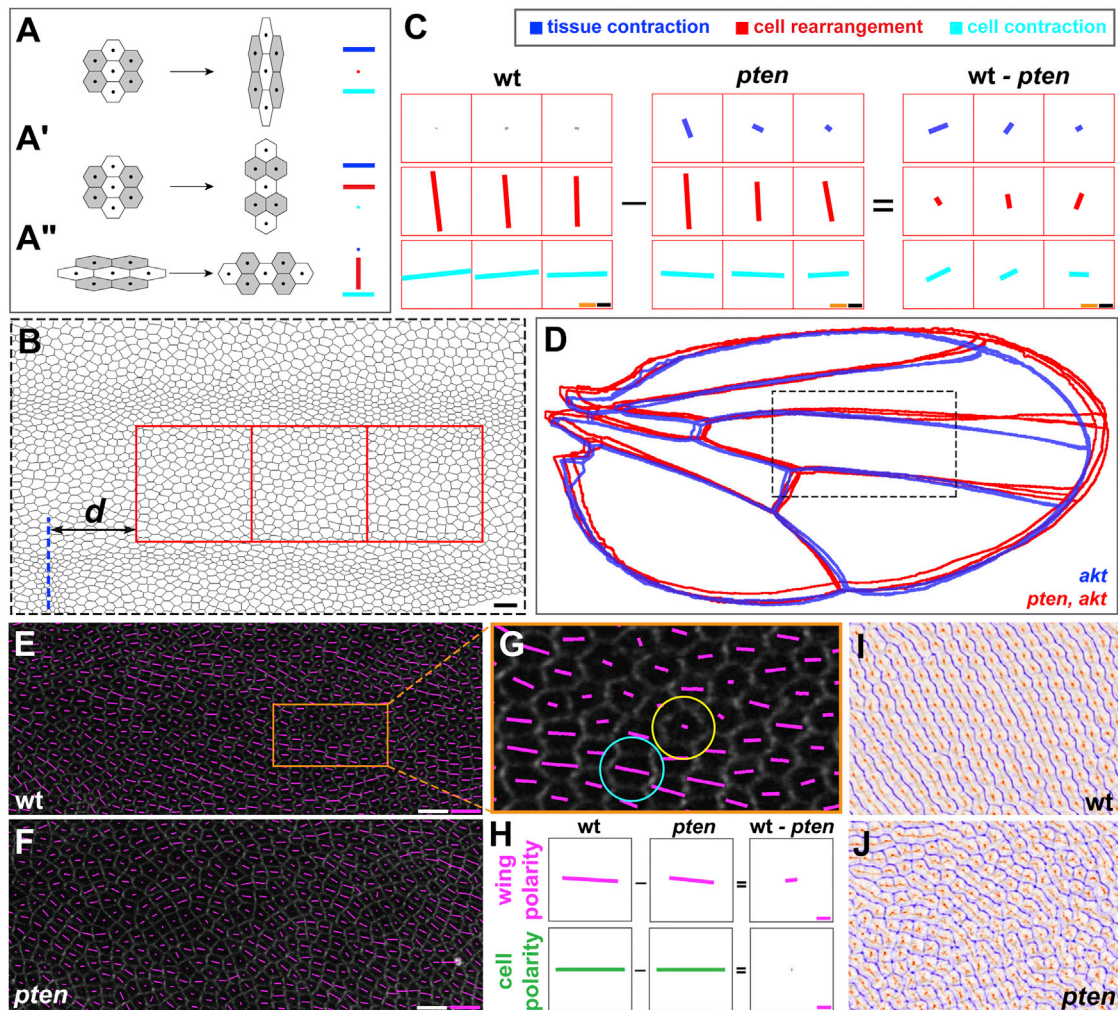


Figure 5. Role of PTEN in Tissue Morphogenesis, PCP, and Tissue Architecture

(A–A'') Framework for quantitative analysis of tissue contraction–extension (blue), cell–cell rearrangements (red), and cell shape changes (cyan; see [Experimental Procedures](#)). (A and A') The patch of tissue undergoes the same contraction–extension through pure cell shape changes (A), and through pure cell rearrangements (A'). (A'') Initial cell elongation vanishes through cell rearrangements occurring in the perpendicular direction and resulting in regular hexagons and no tissue deformation.

(B) Segmented image of wing (29 hAPF). Red square boxes ($54 \times 54 \mu\text{m}^2$) indicate the regions where quantitative analysis was performed. $d = 40 \mu\text{m}$.

(C) Comparative analysis of morphogenesis in WT and *pten* wings. Subtractive analysis (“wt-*pten*”) shows that PTEN loss of function results in weaker cell rearrangements and cell shape changes: (1) oscillating junctions reduce the net contribution of cell rearrangements, and (2) the disruption of junction elongation prevents the complete relaxation of cell elongated shapes into regular hexagons, thus resulting in a weaker oriented contraction of cells in a direction slightly tilted with respect to the PD axis. Overall, this corresponds to a defect of tissue contraction along this direction, which is consistent with wing shape defects observed in (D). Significant data are plotted with thick color bars, nonsignificant data with gray bars (see [Experimental Procedures](#)) (Bosveld et al., 2012), averages done over $n = 2$ WT and $n = 2$ *pten* wings.

(D) Outlines of three adult wings from *akt¹/akt³* flies (blue) and *akt¹/akt³;pten¹¹⁷* flies (red) were overlaid. *akt¹/akt³* tissue do not show packing defects as opposed to *akt¹/akt³;pten¹¹⁷* tissue (Figures S1D and S1F). The comparison of *akt¹/akt³* and *akt¹/akt³;pten¹¹⁷* wings permits to determine the function of *pten* on tissue morphogenesis independently of its role in tissue growth. Dashed box indicates region in (B).

(E and F) Quantification on images of fixed wings at 30 hAPF of local and global PCP of Stbm protein (Stbm-YFP, in gray) in WT (E) and *pten* (F) wings. Each bar (magenta) represents the amplitude and direction of the anisotropy in Stbm junctional localization around each cell.

(G) Close up of a region in (E) showing examples of cells displaying a weak polarity of Stbm intensity resulting in a small bar (yellow circle), and a strong anisotropy yielding a large bar in the direction of polarization (cyan circle). The intensity level (IL) of each pixel in Stbm ($0 < IL < 255$) around the cell cortex was used to characterize cell polarity (see [Experimental Procedures](#)).

(H) Averages of Stbm polarity in WT and *pten* wings. The “wing polarity” characterizes the coordination of cell polarities across the wing. The “cell polarity” quantifies the polarization of Stbm distribution in each cell. Subtractive analysis shows a significant difference in wing polarity between WT and *pten* tissues, but no difference in Stbm cell polarity (average over $n = 3$ WT wings, $n = 3$ *pten* wings, with $\langle n_{\text{cells}} \rangle \approx 1,040$ analyzed cells per wing).

(I and J) Using cuticles refraction microscopy (Doyle et al., 2008), the ridges on adult wing cuticle that characterize the architecture of wing tissue were determined in WT and *pten* tissues. Images are superposition of the dorsal (purple) and the ventral (orange) ridges in WT wings (I) and *pten^{RNAi}* wings (J).

Scale bars represent $10 \mu\text{m}$ (B and C, black bars; E and F, white bars); $2 \mu\text{m}^2 \text{min}^{-1}$ (C, orange bars); $IL = 50$ (E and F), $IL = 2$ (H), magenta bars.

at 25°C before dissection. For *rok* clones, heat shocks were performed 2 days BPF to obtain small clones mostly devoid of very large cells. Ubi-GFP-Rok was generated by cloning under the control of Ubiquitin 63E promoter a full-length *rok* cDNA downstream of GFP in a P element vector. Ubi-GFP-Rok rescues the *rok*² null allele in somatic clones.

Immunostaining

Wing dissection, fixation, and immunostaining were carried out as described (Classen et al., 2008). Antibodies are rat anti-E-cad (1:50; Developmental Studies Hybridoma Bank), mouse anti-FasciclinIII (1:50; DSHB), rat anti-Crumbs (1:1000, gift of U. Tepass), mouse anti-Discs-large (1:1000; DSHB), Alexa Fluor 488-, 555-conjugated secondary antibodies (Molecular Probes), and Cy5-conjugated secondary antibodies (Jackson ImmunoResearch). Images were acquired on a laser-scanning confocal microscope (LSM710, Zeiss).

Time-Lapse Experiments

Timed pupae were dissected, mounted and imaged as previously described for the fly thorax (Gho et al., 1999), acquiring one z stack of images for each channel every 5 min. The en-GAL4 driver was used to express the *pten* dsRNA in the posterior wing. For the time-lapse experiments with E-cad-GFP, Gal80^{ts} was used for temporal control of the dsRNA expression. Larvae were raised at 18°C, and shifted at 29°C 1 day BPF, affecting the PTEN function during pupal development. Developmental times were corrected to match the 25°C reference, using a coefficient of 0.79. Images were acquired with a Ropper spinning-disk confocal mounted on an Eclipse Ti microscope (Nikon) using the Metamorph software.

Laser Ablations

Both wild-type and *pten* mutant clone cells were labeled with E-cad-GFP. A 2-photon Mai-Tai laser (890 nm, 100 mW, 2 repetitions) ablated a cell junction (Hutson and Ma, 2007) on NLO LSM710 (Zeiss). Junction ablations and initial velocity quantifications were carried out as in Bosveld et al. (2012).

Image Treatments, Quantification, Intensity Measurement, and Cell Junction Tracking

For detailed information on image treatments, quantification, intensity measurement, and cell junction tracking, see the [Supplemental Experimental Procedures](#).

SUPPLEMENTAL INFORMATION

Supplemental Information includes Supplemental Experimental Procedures, four figures, and three movies and can be found with this article online at <http://dx.doi.org/10.1016/j.devcel.2013.04.020>.

ACKNOWLEDGMENTS

We thank E. Hafen, H. Hong, R. Kares, E. Martin-Blanco, H. Oda, F. Pichaud, U. Tepass, C. Wilson, E. Wieschaus, J. Zallen, the Developmental Studies Hybridoma Bank, the Bloomington Stock Center, and TRiP at Harvard Medical School (NIH/NIGMS R01-GM084947) for strains and antibodies; the Curie Imaging Facility (PICT-IBISA@BDD); J. Käfer for advice with computer simulations; and V. Hakim, E. Heard, J. Käfer, A.-M. Lennon, and J.-P. Vincent for critical comments on the manuscript. This work is supported by the FRM (26329) and the INCA (4731); by grants to Y.B. from the ARC (4830), the ANR (BLAN07-3-207540, MorphoDro), and an ERC Starting Grant (CePoDro 209718); and by the CNRS, INSERM, and the Curie Institute. P.-L.B. is supported by an INSERM postdoctoral fellowship.

Received: August 4, 2012

Revised: March 12, 2013

Accepted: April 22, 2013

Published: May 23, 2013

REFERENCES

- Aigouy, B., Farhadifar, R., Staple, D.B., Sagner, A., Röper, J.C., Jülicher, F., and Eaton, S. (2010). Cell flow reorients the axis of planar polarity in the wing epithelium of *Drosophila*. *Cell* 142, 773–786.
- Amano, M., Nakayama, M., and Kaibuchi, K. (2010). Rho-kinase/ROCK: a key regulator of the cytoskeleton and cell polarity. *Cytoskeleton* 67, 545–554.
- Bellaïche, Y., Beaudoin-Massiani, O., Stuttem, I., and Schweisguth, F. (2004). The planar cell polarity protein Strabismus promotes Pins anterior localization during asymmetric division of sensory organ precursor cells in *Drosophila*. *Development* 131, 469–478.
- Bertet, C., Sulak, L., and Lecuit, T. (2004). Myosin-dependent junction remodeling controls planar cell intercalation and axis elongation. *Nature* 429, 667–671.
- Bosveld, F., Bonnet, I., Guirao, B., Tlili, S., Wang, Z., Petitalot, A., Marchand, R., Bardet, P.-L., Marcq, P., Graner, F., and Bellaïche, Y. (2012). Mechanical control of morphogenesis by Fat/Dachsous/Four-jointed planar cell polarity pathway. *Science* 336, 724–727.
- Britton, J.S., Lockwood, W.K., Li, L., Cohen, S.M., and Edgar, B.A. (2002). *Drosophila*'s insulin/PI3-kinase pathway coordinates cellular metabolism with nutritional conditions. *Dev. Cell* 2, 239–249.
- Chalhoub, N., and Baker, S.J. (2009). PTEN and the PI3-kinase pathway in cancer. *Annu. Rev. Pathol.* 4, 127–150.
- Clark, K., Langeslag, M., Figdor, C.G., and van Leeuwen, F.N. (2007). Myosin II and mechanotransduction: a balancing act. *Trends Cell Biol.* 17, 178–186.
- Classen, A.K., Anderson, K.I., Marois, E., and Eaton, S. (2005). Hexagonal packing of *Drosophila* wing epithelial cells by the planar cell polarity pathway. *Dev. Cell* 9, 805–817.
- Classen, A.K., Aigouy, B., Giangrande, A., and Eaton, S. (2008). Imaging *Drosophila* pupal wing morphogenesis. *Methods Mol. Biol.* 420, 265–275.
- de Matos Simões, S., Blankenship, J.T., Weitz, O., Farrell, D.L., Tamada, M., Fernandez-Gonzalez, R., and Zallen, J.A. (2010). Rho-kinase directs Bazooka/Par-3 planar polarity during *Drosophila* axis elongation. *Dev. Cell* 19, 377–388.
- Doyle, K., Hogan, J., Lester, M., and Collier, S. (2008). The Frizzled planar cell polarity signaling pathway controls *Drosophila* wing topography. *Dev. Biol.* 317, 354–367.
- Farhadifar, R., Röper, J.C., Aigouy, B., Eaton, S., and Jülicher, F. (2007). The influence of cell mechanics, cell-cell interactions, and proliferation on epithelial packing. *Curr. Biol.* 17, 2095–2104.
- Fernandez-Gonzalez, R., de Matos Simões, S., Röper, J.C., Eaton, S., and Zallen, J.A. (2009). Myosin II dynamics are regulated by tension in intercalating cells. *Dev. Cell* 17, 736–743.
- Gho, M., Bellaïche, Y., and Schweisguth, F. (1999). Revisiting the *Drosophila* microchaete lineage: a novel intrinsically asymmetric cell division generates a glial cell. *Development* 126, 3573–3584.
- Gibson, M.C., Patel, A.B., Nagpal, R., and Perrimon, N. (2006). The emergence of geometric order in proliferating metazoan epithelia. *Nature* 442, 1038–1041.
- Glazier, J.A., and Graner, F. (1993). Simulation of the differential adhesion driven rearrangement of biological cells. *Phys. Rev. E* 47, 2128–2154.
- Graner, F., and Glazier, J.A. (1992). Simulation of biological cell sorting using a two-dimensional extended Potts model. *Phys. Rev. Lett.* 69, 2013–2016.
- Graner, F., and Sawada, Y. (1993). Can surface adhesion drive cell rearrangement? Part II: a geometrical model. *J. Theor. Biol.* 164, 477–506.
- Hales, T.C. (2001). The honeycomb conjecture. *Disc. Comp. Geom.* 25, 1–22.
- Harumoto, T., Ito, M., Shimada, Y., Kobayashi, T.J., Ueda, H.R., Lu, B., and Uemura, T. (2010). Atypical cadherins Dachsous and Fat control dynamics of noncentrosomal microtubules in planar cell polarity. *Dev. Cell* 19, 389–401.
- Hilgenfeldt, S., Eriskin, S., and Carthew, R.W. (2008). Physical modeling of cell geometric order in an epithelial tissue. *Proc. Natl. Acad. Sci. USA* 105, 907–911.

- Hutson, M.S., and Ma, X. (2007). Plasma and cavitation dynamics during pulsed laser microsurgery in vivo. *Phys. Rev. Lett.* **99**, 158104.
- Hutson, M.S., Veldhuis, J., Ma, X., Lynch, H.E., Cranston, P.G., and Brodland, G.W. (2009). Combining laser microsurgery and finite element modeling to assess cell-level epithelial mechanics. *Biophys. J.* **97**, 3075–3085.
- Käfer, J., Hayashi, T., Marée, A.F., Carthew, R.W., and Graner, F. (2007). Cell adhesion and cortex contractility determine cell patterning in the *Drosophila* retina. *Proc. Natl. Acad. Sci. USA* **104**, 18549–18554.
- Keller, R. (2006). Mechanisms of elongation in embryogenesis. *Development* **133**, 2291–2302.
- Knox, A.L., and Brown, N.H. (2002). Rap1 GTPase regulation of adherens junction positioning and cell adhesion. *Science* **295**, 1285–1288.
- Krieg, M., Arboleda-Estudillo, Y., Puech, P.H., Käfer, J., Graner, F., Müller, D.J., and Heisenberg, C.P. (2008). Tensile forces govern germ-layer organization in zebrafish. *Nat. Cell Biol.* **10**, 429–436.
- Lecuit, T., and Lenne, P.F. (2007). Cell surface mechanics and the control of cell shape, tissue patterns and morphogenesis. *Nat. Rev. Mol. Cell Biol.* **8**, 633–644.
- Lecuit, T., Lenne, P.F., and Munro, E. (2011). Force generation, transmission, and integration during cell and tissue morphogenesis. *Annu. Rev. Cell Dev. Biol.* **27**, 157–184.
- Li, Z., Dong, X., Wang, Z., Liu, W., Deng, N., Ding, Y., Tang, L., Hla, T., Zeng, R., Li, L., and Wu, D. (2005). Regulation of PTEN by Rho small GTPases. *Nat. Cell Biol.* **7**, 399–404.
- Ma, D., Amonlirdviman, K., Raffard, R.L., Abate, A., Tomlin, C.J., and Axelrod, J.D. (2008). Cell packing influences planar cell polarity signaling. *Proc. Natl. Acad. Sci. USA* **105**, 18800–18805.
- Maitre, J.L., Berthoumieux, H., Krens, S.F., Salbreux, G., Jülicher, F., Paluch, E., and Heisenberg, C.P. (2012). Adhesion functions in cell sorting by mechanically coupling the cortices of adhering cells. *Science* **338**, 253–256.
- Martin-Belmonte, F., Gassama, A., Datta, A., Yu, W., Rescher, U., Gerke, V., and Mostov, K. (2007). PTEN-mediated apical segregation of phosphoinositides controls epithelial morphogenesis through Cdc42. *Cell* **128**, 383–397.
- McGuire, S.E., Le, P.T., Osborn, A.J., Matsumoto, K., and Davis, R.L. (2003). Spatiotemporal rescue of memory dysfunction in *Drosophila*. *Science* **302**, 1765–1768.
- McKenzie, E., Krupin, A., and Kelley, M.W. (2004). Cellular growth and rearrangement during the development of the mammalian organ of Corti. *Dev. Dyn.* **229**, 802–812.
- Narimatsu, M., Bose, R., Pye, M., Zhang, L., Miller, B., Ching, P., Sakuma, R., Luga, V., Roncari, L., Attisano, L., and Wrana, J.L. (2009). Regulation of planar cell polarity by Smurf ubiquitin ligases. *Cell* **137**, 295–307.
- Nishimura, T., Honda, H., and Takeichi, M. (2012). Planar cell polarity links axes of spatial dynamics in neural-tube closure. *Cell* **149**, 1084–1097.
- Nowak, R.B., Fischer, R.S., Zoltoski, R.K., Kuszak, J.R., and Fowler, V.M. (2009). Tropomodulin1 is required for membrane skeleton organization and hexagonal geometry of fiber cells in the mouse lens. *J. Cell Biol.* **186**, 915–928.
- Oda, H., and Tsukita, S. (2001). Real-time imaging of cell-cell adherens junctions reveals that *Drosophila* mesoderm invagination begins with two phases of apical constriction of cells. *J. Cell Sci.* **114**, 493–501.
- Papusheva, E., and Heisenberg, C.P. (2010). Spatial organization of adhesion: force-dependent regulation and function in tissue morphogenesis. *EMBO J.* **29**, 2753–2768.
- Perez, T.D., Tamada, M., Sheetz, M.P., and Nelson, W.J. (2008). Immediate-early signaling induced by E-cadherin engagement and adhesion. *J. Biol. Chem.* **283**, 5014–5022.
- Pickering, K., Alves-Silva, J., Goberdhan, D., and Millard, T.H. (2013). Par3/Bazooka and phosphoinositides regulate actin protrusion formation during *Drosophila* dorsal closure and wound healing. *Development* **140**, 800–809.
- Pinal, N., Goberdhan, D.C., Collinson, L., Fujita, Y., Cox, I.M., Wilson, C., and Pichaud, F. (2006). Regulated and polarized PtdIns(3,4,5)P₃ accumulation is essential for apical membrane morphogenesis in photoreceptor epithelial cells. *Curr. Biol.* **16**, 140–149.
- Rauzi, M., Verant, P., Lecuit, T., and Lenne, P.F. (2008). Nature and anisotropy of cortical forces orienting *Drosophila* tissue morphogenesis. *Nat. Cell Biol.* **10**, 1401–1410.
- Rauzi, M., Lenne, P.F., and Lecuit, T. (2010). Planar polarized actomyosin contractile flows control epithelial junction remodelling. *Nature* **468**, 1110–1114.
- Rivard, N. (2009). Phosphatidylinositol 3-kinase: a key regulator in adherens junction formation and function. *Front. Biosci.* **14**, 510–522.
- Royou, A., Field, C., Sisson, J.C., Sullivan, W., and Karess, R. (2004). Reassessing the role and dynamics of nonmuscle myosin II during furrow formation in early *Drosophila* embryos. *Mol. Biol. Cell* **15**, 838–850.
- Staple, D.B., Farhadifar, R., Röper, J.-C., Aigouy, B., Eaton, S., and Jülicher, F. (2010). Mechanics and remodelling of cell packings in epithelia. *Eur. Phys. J. E. Soft Matter.* **33**, 117–127.
- Stocker, H., Andjelkovic, M., Oldham, S., Laffargue, M., Wymann, M.P., Hemmings, B.A., and Hafen, E. (2002). Living with lethal PIP₃ levels: viability of flies lacking PTEN restored by a PH domain mutation in Akt/PKB. *Science* **295**, 2088–2091.
- Tardieu, A. (1988). Eye lens proteins and transparency: from light transmission theory to solution X-ray structural analysis. *Annu. Rev. Biophys. Biophys. Chem.* **17**, 47–70.
- Togashi, H., Kominami, K., Waseda, M., Komura, H., Miyoshi, J., Takeichi, M., and Takai, Y. (2011). Nectins establish a checkerboard-like cellular pattern in the auditory epithelium. *Science* **333**, 1144–1147.
- Warrington, S.J., Strutt, H., and Strutt, D. (2013). The Frizzled-dependent planar polarity pathway locally promotes E-cadherin turnover via recruitment of RhoGEF2. *Development* **140**, 1045–1054.
- Winter, C.G., Wang, B., Ballew, A., Royou, A., Karess, R., Axelrod, J.D., and Luo, L. (2001). *Drosophila* Rho-associated kinase (Drok) links Frizzled-mediated planar cell polarity signaling to the actin cytoskeleton. *Cell* **105**, 81–91.
- Xu, T., and Rubin, G.M. (1993). Analysis of genetic mosaics in developing and adult *Drosophila* tissues. *Development* **117**, 1223–1237.
- Yamada, S., and Nelson, W.J. (2007). Localized zones of Rho and Rac activities drive initiation and expansion of epithelial cell-cell adhesion. *J. Cell Biol.* **178**, 517–527.
- Zallen, J.A., and Wieschaus, E. (2004). Patterned gene expression directs bipolar planar polarity in *Drosophila*. *Dev. Cell* **6**, 343–355.

Supplemental Information

PTEN Controls Junction Lengthening and Stability

during Cell Rearrangement in Epithelial Tissue

Pierre-Luc Bardet, Boris Guirao, Camille Paoletti, Fanny Serman, Valentine Léopold, Floris Bosveld, Yûki Goya, Vincent Mirouse, François Graner, and Yohanns Bellaïche

Supplemental Information Guide

Figures S1, related to Figure 1.

This figure shows that PTEN regulates cell packing independently of its roles in cell growth and polarization. It includes PI3K overexpression inducing a phenotype similar to *pten*, genetic epistatic experiments showing that the *pten* phenotype is not due to Akt over-activation, statistical analysis of apical cell sizes showing no effect of *pten* before 30 hAPF and that Rheb-induced overgrowth does not cause cell packing defects. This figure also includes images showing that loss of PTEN does not affect apical-basal polarity and that its packing phenotype is independent of Baz function.

Figure S2, related to Figure 2.

This figure shows essential results of the cellular network model and the fitting graphs used to determine the range of values of side parameters in wt and *pten* tissues. It also shows that only the junctions of the *pten* cells exhibit the short-junctions phenotype, regardless of the clone size.

Figure S3, related to Figure 3.

This figure shows that *pten* packing defects arise concomitantly to cell rearrangements, and independently of cell proliferation delay. It also illustrates how cell rearrangements were counted. Finally, it helps to show that short time variations in MyosinII intensity at junctions precede variations of their lengths, ruling out a passive dilution of MyosinII upon junction elongation.

Figure S4, related to Figure 4.

This figure shows the increase of PIP₃ in the *pten* tissue. It also demonstrates that loss of Rok reduced MyoII cortical distribution in wt and *pten* contexts. Finally, it shows that final simulated cellular packings do not depend on the genotype of the tissue image used as initial state of the simulations.

Movie S1, related to Figure 3.

This movie shows that the differences between wt and *pten* cell patterns increase over time.

Movie S2, related to Figure 3.

This movie illustrates typical cell rearrangements in wt (A) and *pten* (B) tissue as well as how they were scored in our study. It also illustrates how MyoII transiently accumulates at the

shortening and elongating junctions during cell rearrangements in wt tissue (C) but remains accumulated at the short junctions after cell rearrangements in *pten* tissue (D).

Movie S3, related to Figure 4.

This movie illustrates the evolution of two computer simulations of wt and *pten* tissues showing that the maintenance of high cortical tension is sufficient to account for the *pten* packing phenotype.

Supplemental Experimental Procedures

This section includes the additional experimental procedures used in the paper:

- Numerical simulations.
- Analysis of temporal correlation between MyosinII-GFP intensity and junction length.
- Quantitative analysis of wing morphogenesis.
- Quantitative analysis of PCP organization in the wing.
- Theoretical model of ordered cellular packing.

Supplemental References

This section includes all the references cited in the supplemental information.

Supplemental Information

1 - Supplemental Figure and Legends

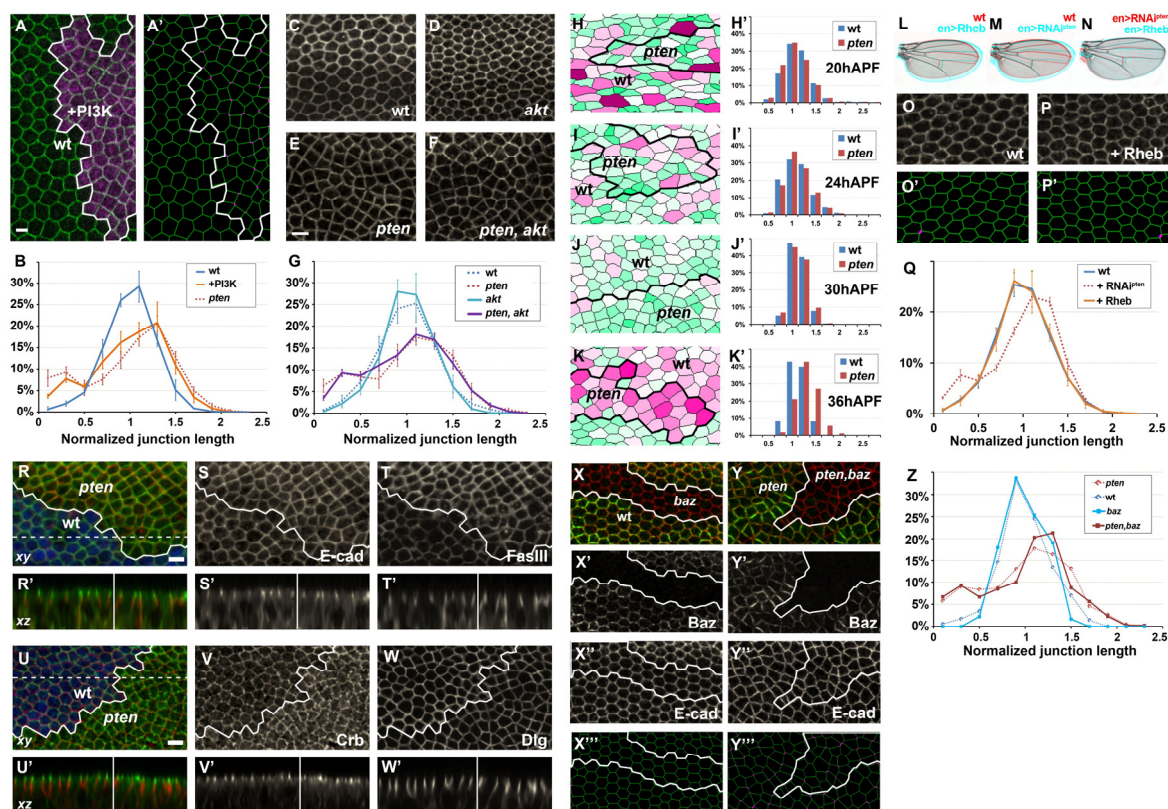


Figure S1, related to Figure 1: *pten* cell packing phenotype is not due to a cell growth or cell polarity defect.

(A-B) Confocal image (A) and segmented image (A') of a clone of cells overexpressing the catalytic subunit of PI3K (dp110). Overexpressing cells are labeled by mRFP expression (magenta in A) and clone boundary is outlined by a white line (A-A'). Cell apical junctions are outlined with armadillo-GFP (arm-GFP, green in A). Short sides ($< 0.5 \times$ average length) are in magenta (A'). (B) Histogram of the junction length distribution normalized by average length of wt, *pten*¹ and overexpressing PI3K (PI3K^{over}) cells. PI3K^{over}: 19 clones on 2 wings, 1149 sides; wt tissue surrounding the PI3K overexpressing clones on 2 wings, 2190 sides. *pten*¹: 8 clones in 3 wings, 4329 sides.

(C-G) The activation of the Akt kinase depends on its membrane recruitment driven by the interaction of its PH domain with PIP3 (Chalhoub and Baker, 2009). Akt overactivation is thought to be responsible for most of the adverse effects of PTEN loss of function both in cancer and animal model (Stocker et al., 2002). Accordingly, lethality and defects in apical surface formation in *Drosophila* rhabdomere caused by the loss of PTEN function are rescued by reducing the binding of Akt to PIP3

via a specific *akt¹/akt³* allelic combination (Pinal et al., 2006; Stocker et al., 2002). We therefore examined cell packing in double *akt¹/akt³, pten* mutant flies to determine whether the loss of PTEN function triggers defects in cell packing by over-activating Akt. **(C-F)** Confocal images of E-cadherin staining at 30h APF in wt **(C)** tissue, *akt¹/akt³* mutant tissue **(D)**, *pten¹¹⁷* mutant clone **(E)** and double *akt¹/akt³, pten¹¹⁷* mutant tissues **(F)**. **(G)** Histogram of the junction length distributions normalized by average length in wt tissue, *akt¹/akt³* mutant tissue, *pten¹¹⁷* mutant clone and double *akt¹/akt³, pten¹¹⁷* mutant tissue. As previously reported (Stocker et al., 2002), we observed a rescue of lethality and animal size in *akt¹/akt³, pten¹¹⁷* double mutant combination, yet single *pten¹¹⁷* tissue **(E)** and double *akt¹/akt³, pten¹¹⁷* tissue **(F)** were characterized by similar cell packing defects and side length distribution **(G)**. Hence, reduction of Akt function did not rescue the PTEN loss of function packing defects, establishing that PTEN packing defects are not a consequence of Akt overactivation and overgrowth. wt: 3 wings, 6955 sides, *pten¹¹⁷*: 3 wings, 4329 sides; *akt¹/akt³*: 1 wing, 4339 sides; *akt¹/akt³, pten¹¹⁷*: 2 wings, 6046 sides.

(H-K') Apical size areas of *pten* cells and surrounding control cells at 20 hAPF, 24 hAPF, 30 hAPF and 36h APF. For each time-point, typical segmented images are shown **(H-K)**, where the area of each cell is indicated by colors, ranging linearly from dark purple for largest cells (area > 25 μm^2) to dark green for smallest cells (area < 5 μm^2). The right panels **(H'-K')** show the histogram of the distribution of the cell area normalized by their average in *pten* (red) and the surrounding wt (blue) tissues. No significant difference ($p > 0.05$) in apical size area distribution are observed at 20h **(H-H')**, 24h **(I, I')** and 30h APF **(J, J')** between control and *pten¹* cells. At 36h APF **(K-K')**, after the final cell packing is reached, *pten* cells are significantly larger than their wt control ($p < 10^{-10}$). This is consistent with previous report showing bigger *pten* cells in adult wings (Goberdhan et al., 1999). 20h APF : 4 clones on 3 wings, wt : 640 cells, *pten* : 579 cells. 24h APF : 3 clones on 2 wings, wt : 873 cells, *pten* : 700 cells. 30h APF : 4 clones on 3 wings, wt : 1117 cells, *pten* : 753 cells. 36h APF : 6 clones on 3 wings, wt : 1247 cells, *pten* : 600 cells.

(L-Q) Rheb is a downstream effector of PTEN in the cell growth pathway involving TSC1/2 (Patel et al., 2003). Its overexpression in the posterior compartment of the wing induces an overgrowth similar to the one of *pten* loss of function **(L-N)**, but not packing defect **(O-Q)**. Rheb and *pten^{RNAi}* were both expressed using the engrailed Gal4 driver (en>Rheb and en> *pten^{RNAi}*, respectively). Overlay of wt (red in **L, M**), Rheb overexpressing (blue in **L,N**) and *pten^{RNAi}* (blue in **M**; red in **N**) adult wing. **(O-P')** Confocal images **(O-P)** and segmented images **(O'-P')** of regions of cells either control **(O-O')** or overexpressing Rheb **(P-P')**. E-cad staining outlines cell apical junctions (grey in **O-P**), and was skeletonized to obtain panels O' and P' (short sides (< 0.5 x average length) are shown in magenta). **(Q)** Histogram of the junction lengths distributions normalized by average length: wt (blue), *pten¹* (dotted red) and overexpression of Rheb (orange).

(R-W') Confocal in sections in *xy* plane of wing interveins at 30h APF with *pten¹* mutant clones marked by the absence of GFP (blue in **R** and **U**), outlined in white **(R-W)**. The corresponding *xz*

apical-basal sections along the dashed lines (**R**, **U**) are shown below (**R'-W'**); vertical white lines indicate clone boundaries (left wt tissue; right *pten* tissue). (**R-T'**) Localization of the apical marker E-cadherin (E-cad green in **R-R'**; gray in **S-S'**) and basal marker Fasciclin III (Fas III red in **R-R'**; gray in **T-T'**). (**U-W'**) Localization of the apical determinant Crumbs (Crb green in **U-U'**; gray in **V-V'**) and basal determinant Discs-large (Dlg red in **U-U'**; gray in **W, W'**). None of these markers as well as Baz and aPKC (not shown) see their position shifted along the *z*-axis in *pten* compared to wt tissue (**R'-T'**, **U'-W'**).

(**X-Y'''**) Confocal images (**X-X''** and **Y-Y''**) and segmented images (**X'''**, **Y'''**) of *baz* mutant clones within either a wt tissue (wt, **X-X'''**) or a tissue expressing a RNAi against *pten* (*pten*, **Y-Y'''**). Clones were identified by the absence of cytoplasmic GFP (not shown) and of Baz staining (green in **X, Y**; gray in **X', Y'**) and are shown by a white outline (**X-Y'''**). Cell apical contours were labeled by E-cad staining (red in **X, Y**; gray in **X'', Y''**). Short sides (< 0.5 x average length) in magenta (**X'''**, **Y'''**). Loss of Baz function did not affect the honeycomb-like pattern (**X-X'''**). Loss of Baz function in a *pten*^{RNAi} tissue did not prevent cells from forming cobblestone-like patterns (**Y''**) and short junctions (**Y'''**). (**Z**) Histogram of the junction length distributions normalized by average length in wt tissue and in *pten*^{RNAi}, *baz*^{Xi106} or double *pten*^{RNAi}, *baz*^{Xi106}, mutant tissues. The side length distributions in wt and *pten* tissues were unaffected by the loss of Baz function. wt: 342 sides; *baz*^{Xi106}: 178 sides; *pten*^{RNAi}: n=828 sides; *pten*^{RNAi}, *baz*^{Xi106}: 389 sides.

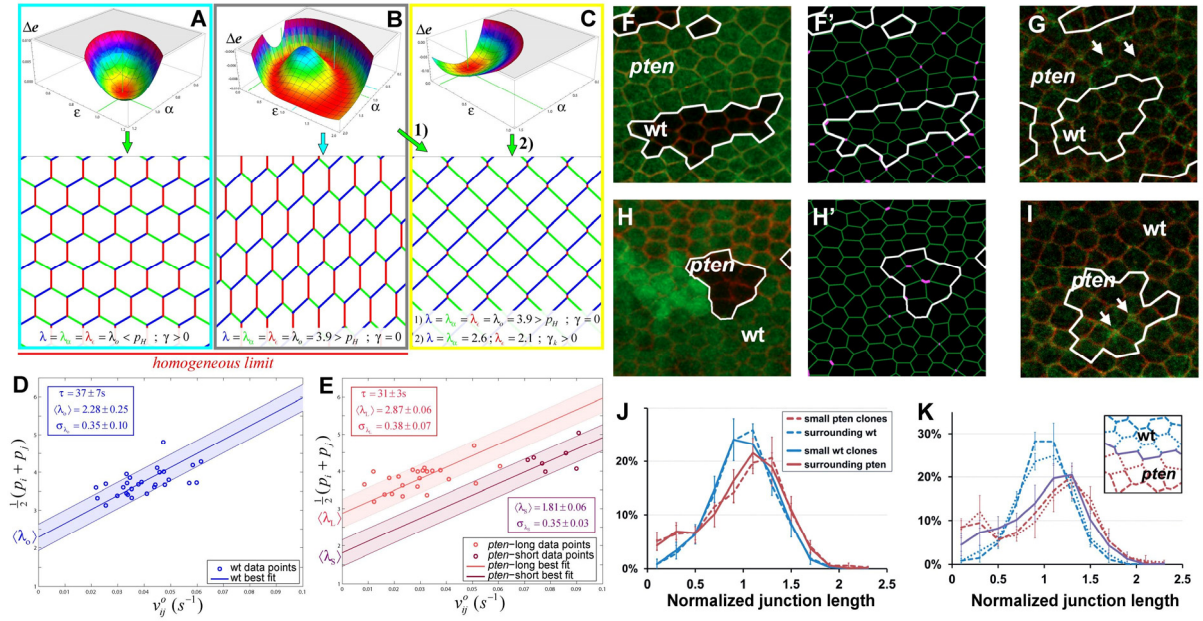


Figure S2, related to Figure 2: Cellular patterns with homogeneous/heterogeneous side properties and inference of theoretical model parameters: only junctions involving *pten* cells remain short, regardless of the size of the clone.

(A-C) Energy landscape Δe as a function of asymmetry parameters (α, ϵ) [eq. (11)] and representation of cellular patterns corresponding to energy minimum for different side parameters triplets $(\lambda, \lambda_\alpha, \lambda_\epsilon)$.

(A) Homogeneous case at *low* side parameter ($\lambda = \lambda_\alpha = \lambda_\epsilon = \lambda_o < p_H$): the energy minimum is unique and corresponds to a honeycomb pattern with $\gamma > 0$.

(B) Homogeneous case at *high* side parameter ($\lambda = \lambda_\alpha = \lambda_\epsilon = \lambda_o > p_H$): the honeycomb pattern now corresponds to a local maximum surrounded by a valley of minima. All configurations in the valley thus have same energy (degenerate), and $\gamma = 0$. We represent two configurations corresponding to two different minima in the valley (cyan and green arrows).

(C) Heterogeneous case. One side (in red) has *lower* side parameter (case 2: $\lambda = \lambda_\alpha = 2.6; \lambda_\epsilon = 2.1$). The energy minimum is unique, and at mechanical equilibrium, this side is shorter and under higher tension. This pattern is exactly the same as the second minima presented in B (green arrow) and is similar to local arrangements in *pten* tissue (in orange in Figure 1B).

(D) Determination of side parameter experimental value in wt tissue by a linear fit to $\frac{1}{2}(p_i + p_j)$ vs. v_{ij}^o data points [eq. (17)]. The fit procedure yielded the characteristic time τ , mean side parameter $\langle \lambda_o \rangle$ value and dispersion around this value σ_{λ_o} . Here we plotted the best fit line with its dispersion domain ($\pm \sigma_{\lambda_o}$) (in blue), and experimental data points for ablated side lengths within the range $\langle l \rangle^{WT} \pm 1.2 \sigma_l^{WT}$ (blue circles).

(E) Determination of side parameter in *pten* tissue using the same fit procedure as in wt **(D)**. This yielded the characteristic time τ , the two mean side parameter values $\langle \lambda_L \rangle, \langle \lambda_S \rangle$ and dispersions around these values $\sigma_{\lambda_L}, \sigma_{\lambda_S}$ for long and short sides, respectively. Here we plotted the best fit lines with their dispersion domains, and data points for ablated side lengths within the range $\langle l \rangle_L^{pten} \pm 1.2\sigma_L^{pten}$ and $\langle l \rangle_S^{pten} \pm 3\sigma_S^{pten}$ (in red and crimson, respectively).

(F-I) Typical images of small wt clones in wings mostly mutant for *pten* **(F-G)**, and small clones mutant for *pten* in wings mostly wt **(H-I)**. Clone boundaries are depicted by a white line **(F-I)**, and by the absence of GFP (green in **F, H**). E-cad staining outlines cell apical junctions (red in **F, G, H, I**), and yielded segmented images **F'** and **H'** [Short sides ($< 0.5 \times$ average length) are shown in magenta]. MyoII (green in **G, I**) distribution is homogenous in small wt tissue region **(G)** surrounded by large *pten* mutant domains, where MyoII distribution is heterogeneous **(G, arrows)**. MyoII distribution is heterogeneous in small *pten* clones **(I, arrows)** and not in the surrounding wt tissue **(I)**.

(J) Histogram of the junction lengths, normalized by the average length, of small clones mutant for *pten* (red dashed line) in wings mostly wt (blue dashed line), and small wt clones (blue solid line) in wings mostly mutant for *pten* (red solid line). Small *pten* clones: 26 clones in 3 wings, average cell number: 22 cells (from 6 to 50), 1162 sides. Surrounding wt: 3680 sides. Small wt clones : 69 clones on 4 wings, average cell number : 10 cells (from 2 to 40), 812 sides. Surrounding *pten*: 3602 sides.

(K) Histogram of the junction lengths, normalized by the average length, of junctions at the border between wt and *pten*¹ mutant tissues. We separately quantified the distribution of the junctions between *pten*¹ and wt cells (purple line). To check for non-autonomous effects, we also quantified the junctions between the wt cells touching *pten*¹ cells and their wt neighbors (blue dotted line), as well as the junctions between the *pten*¹ cells touching wt cells and their *pten*¹ neighbors (red dotted line). For comparison, distributions of junction between wt cells (blue dashed lines) and between *pten* cells (red dashed lines) are shown. Quantifications were performed on the same material as for *pten*¹ in figure 1F.

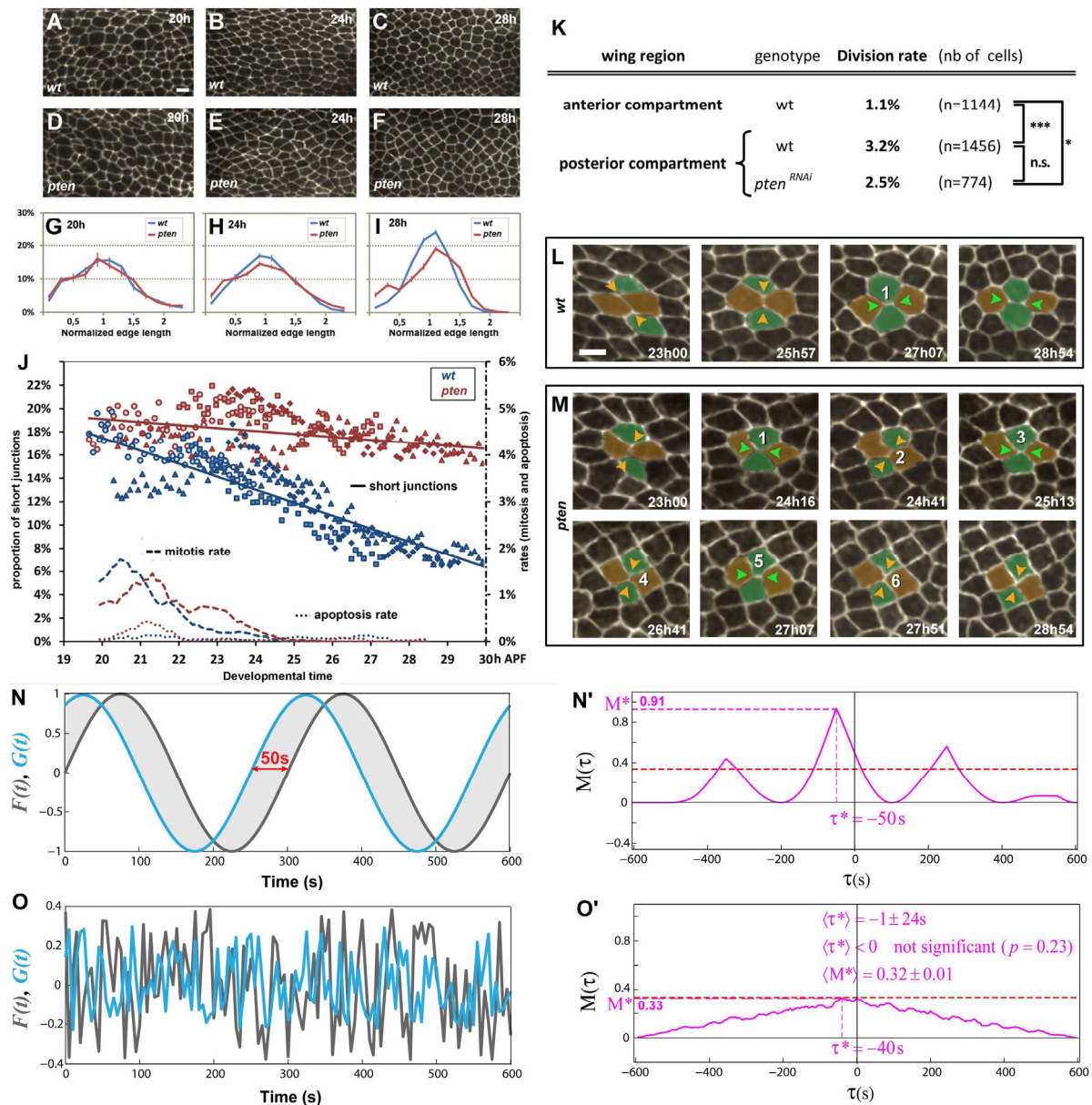


Figure S3, related to Figure 3: Loss of *pten* phenotype is associated with cell rearrangement defects - Temporal correlative analysis of reference functions

(A-F) Images extracted from time-lapse experiments, where apical cell junctions were marked by E-cad-GFP. Expression of the *pten* RNAi was induced 24 h before pupa formation in the posterior part of the wing using the engrailed-Gal4 driver. Typical anterior wt (A-C) and posterior *pten* (D-F) regions are shown at 20 hAPF (A, D), 24 hAPF (B, E) and 28 hAPF (C, F). Although no obvious difference could be seen at 20 hAPF (compare A and D), the wt and *pten* cell packings appeared slightly different at 24 hAPF (compare B and E) and strikingly different at 28 hAPF (compare C and F).

(G-I) Histograms of junction length distributions of wt and *pten* regions in the same wings at 20, 24 and 28 hAPF. Histogram values were averaged over 5 time points around the indicated time [bars

represent dispersion (sd)]. The difference between wt and *pten* junction length distributions increased from 20 to 28 hAPF.

(J) Graph showing the proportion of short sides ($<0.5 \times$ average length), the mitosis and apoptosis rates from 19 to 29 hAPF in wt and *pten* tissues. The proportion of short junctions was measured on four partially overlapping E-Cad time-lapse movies and represented by circles, squares, triangles and diamonds, respectively (blue, wt anterior compartments; red, *pten*^{RNAi} posterior compartments). Linear fits of the proportions of short sides show general tendencies, namely an almost constant proportion of short sides in *pten* tissue, while in wt tissue this proportion decreases as the tissue adopts a honeycomb-like packing. The rates of apoptosis (dotted lines) and mitosis (dashed lines) measured in the same movies were averaged over 9 time points (blue, wt anterior compartments; red, *pten*^{RNAi} posterior compartments). For each time point of each movie, $200 < n < 500$ sides.

(K) Table of the division rate after 23h APF in two wt anterior compartments and two posterior compartments expressing an RNAi against *pten* under the control of the engrailed driver. Although very few mitosis take place at this time, a slight delay in the termination of mitosis is found between the posterior compartments and anterior compartments ($p=4 \cdot 10^{-4}$). The rate of mitosis in the wt and *pten*^{RNAi} posterior compartments are similar ($p=0.31$) showing that PTEN loss of function does not affect the division rate between 23 and 30 hAPF.

(L-M) Images extracted from time-lapse experiments, where apical cell junctions were marked by E-cad-GFP in wt (**L**) and *pten* (**M**) tissues. Four cells involved in a cell rearrangement are labeled in brown (adjacent cells at 23h00 APF) and green (non-adjacent cells at 23h00 APF) in wt (**L**) or *pten* (**M**) tissues. Cell rearrangements bring the green cells in contact, leading to the formation of new cell junctions (at 27h07 APF in E; at 24h16 APF in F). Junctions that are remodeled during the tracked rearrangement are pointed out by two arrowheads, which color matches the one of the touching cells (green or orange). In the wt tissue, the newly-formed junction regrew and was stable after rearrangement (**L**). In contrast, the *pten* cells never regrew a long junction, but instead kept rearranging, giving rise to short junctions and cobblestone patterns (**M**).

(N-N') Example of temporal correlative analysis of two offset sines. (N) Plotted functions are $F(t) = \sin \omega t$ (gray) and $G(t) = \sin \omega(t + \tau_0) = F(t + \tau_0)$ (blue), with $\omega = 4\pi/T_{\max}$ where $T_{\max} = 600$ s is the time of imaging, and temporal offset $\tau_0 = 50$ s (indicated in red). G is in advance on F by $\tau_0 = 50$ s, since G has the value at time t that F will only reach at $t + \tau_0 > t$. The area between the two curves is highlighted in light gray. (N') The delay function $M(\tau)$ of two functions $F(t)$ and $G(t)$ aims at determining the time delay τ in interval $[T_{\max}, -T_{\max}]$ that corresponds to the best match between $F(t)$ and $G(t + \tau)$, namely the delay τ that minimizes the area between $F(t)$ and $G(t + \tau)$ curves (see Extended Experimental Procedures). Taking functions F and G given in (N) as example, $M(\tau)$ reaches maximum $M^*=0.91$ when this area is minimum, which occurs here for the optimal time

delay $\tau^* = -\tau_0 = -50$ s. Indeed, the two curves then perfectly overlap since $G(t + \tau^*) = F(t + \tau_0 + \tau^*) = F(t)$. Dashed red line corresponds to a threshold indicating the absence of correlation between F and G (see **O-O'**).

(O-O') Temporal correlative analysis performed on two uncorrelated functions F and G taking random values in the respective domains $[-0.38, 0.38]$ and $[-0.26, 0.26]$ that correspond to the average domains of variations of dimensionless length and MyoII intensity measured in our 8 experiments, respectively (O). In such cases, $M(\tau)$ does not display any noticeable peak, resulting in large uncertainty in the determination of the optimal time delay τ^* (O'). The analysis of 1000 simulated couples (F, G) of such uncorrelated functions yielded as expected strong variations around the mean $\langle \tau^* \rangle$ (O'). We found $\langle M^* \rangle = 0.32 \pm 0.01$ and thus took $M_{\text{rand}} = 0.33$ (dashed red line) to define a threshold on M^* below which F and G were considered not correlated.

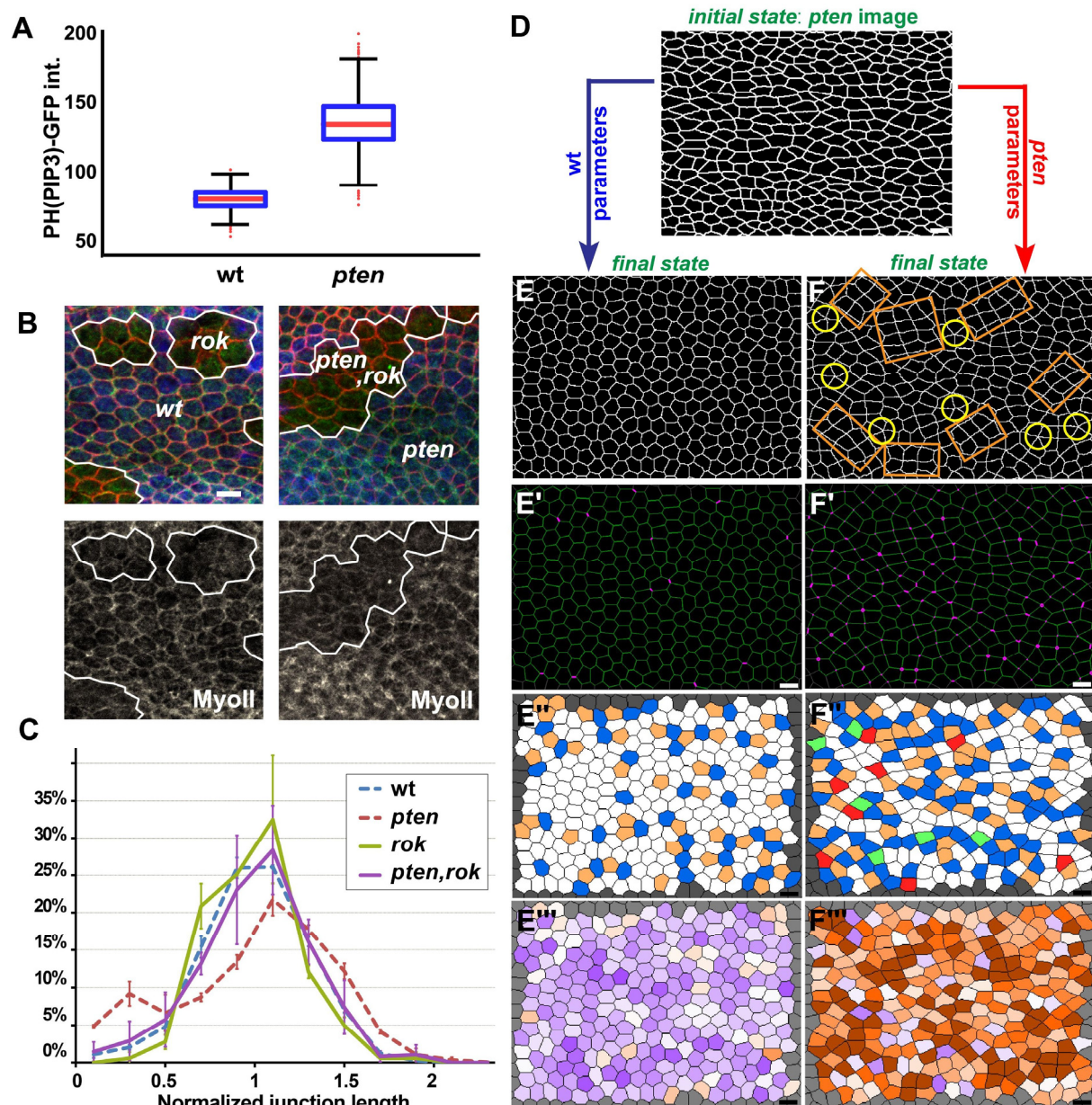


Figure S4, related to Figure 4: Maintenance of cortical tension during cell rearrangements is necessary and sufficient to explain the *pten* packing phenotype.

(A) Box plot of the PH(PIP3)-GFP signal in wt and *pten*^{RNAi} tissues ($p < 10^{-10}$, t-student test).

(B) Confocal images of *rok*² clones in *pten*^{RNAi} (right panels) or a wt tissue (left panels). Clones boundaries were identified by the absence of nuclear mRFP (blue in upper panels) and are outlined by white lines. Cells apical contours were labeled by E-cad staining (red in upper panels) and MyoII was revealed by the localization of the GFP fusion Myo-GFP (green in upper panels; gray in lower panels). In wt and in *pten*^{RNAi} tissue, loss of Rok function led to an important decrease in MyoII-GFP staining.

(C) Histograms of junction length distributions in wt cells and in *pten*^{RNAi}, *rok*² and double *pten*^{RNAi}, *rok*² cells. Quantifications were performed on wt: 897 sides; *pten*^{RNAi}: 1669 sides; *rok*²: 185 sides; *pten*^{RNAi}, *rok*²: 299 sides.

(D-F''') Numerical simulations based on the cellular Potts model of wt and *pten* tissues.

(D) Segmented experimental image of *pten* tissue at 24 hAPF used as initial state of both simulations using parameters of wt (blue arrow) and *pten* (red arrow).

(E-E''') Typical final state of simulations run with wt parameters resulting in a honeycomb-like packing (**E**) and displaying very few short junctions (**E'**), a small disorder in number of neighbors (**E''**) and a low junction length heterogeneity (**E'''**).

(F-F''') Typical final state of simulations run with *pten* parameters resulting in a packing displaying cobblestone (orange) and rosette (yellow) patterns (**F**), and many short junctions (**F'**), a large disorder of number of neighbors (**F''**) and a large junction length heterogeneity (**F'''**).

Scale bars = 5 μm .

2 - Supplemental Movie Legends

Movie S1, related to Figure 3: Differences between wt and *pten* cell packings increase over time

Two extracts of one time-lapse movie where apical cell outlines are marked by E-cad-GFP, showing anterior wt (upper left panel) and posterior *pten* (lower left panel), from 20 to 31 hAPF at 29°C. Some cobblestone (orange) and rosette (yellow) patterns are highlighted in last image. The right panel shows the histograms of the junction length distributions in wt (blue) and *pten* (red) tissues, taking into account 4 partially overlapping films. The *pten* and wt distributions become statistically different from 22 hAPF onwards ($p < 0.01$). Histogram values were averaged over 5 timepoints around the indicated time [bars represent dispersion (sd)]. $n > 400$ sides per timepoint per genotype.

Movie S2, related to Figure 3: Cell rearrangements and MyoII accumulation in wt and *pten* tissues

(A) Typical cell rearrangements in wt. Close-up on four cells of a time-lapse movie where apical cell outlines are marked by the E-cad-GFP in the anterior wt compartment, from 23 to 29 hAPF at 29°C. This illustrates how cell rearrangements were scored and shows how a junction regrows after a neighbor exchange in wt tissue.

(B) Typical cell rearrangements in *pten*. Close-up on four cells of a time-lapse movie where apical cell outlines are marked by the fusion protein E-cad-GFP in the posterior *pten* compartment, from 23 to 29 hAPF at 29°C. This illustrates how cell rearrangements were scored and shows how a junction, failing to regrow after a neighbor exchange, frequently vanishes via another cell rearrangement in *pten* tissue.

(C) MyoII transiently accumulates at the shortening and elongating junctions during cell rearrangements in wt tissue. Extract of a time-lapse movie where the fusion proteins Baz:Cherry and MyoII-GFP are expressed in a wt wing at 25°C, from 25 to 30 hAPF. Two typical examples are highlighted, where shrinking junctions are marked with boxed brackets, 4-fold vertices with circles and resulting stable long junctions with parentheses.

(D) MyoII steadily accumulates at the short junctions after cell rearrangements in *pten* tissue. Posterior compartment of a wing expressing a RNAi against *pten*, together with the Baz-Cherry and MyoII-GFP at 25°C, from 25 to 30 hAPF. Two typical examples are highlighted, where shrinking junctions are marked with boxed brackets, 4-fold vertices and very short sides that fail to regrow with circles.

Movie S3, related to Figure 4: Numerical simulations of wt and *pten* wing tissues

(A-B'') Simulations both starting from the same segmented experimental image of a wt tissue, run with wt parameters (A-A'') and *pten* parameters (B-B''). Cell sides wiggle because of fluctuations which amplitude is set in the simulations (Extended Experimental Procedures). These fluctuations

favor the exploration of energy landscape and the relaxation of the initial packing into a more stable cell packing with lower energy. Last images of the movie correspond to Figures 4N and 4O, respectively. (**A',B'**) Evolution of short junctions during the simulations ($l \leq 0.5$ in magenta, $l > 0.5$ dark green). The last set of images correspond to Figures 4N' and 4O', respectively. (**A'',B''**) Evolution of the number of neighbors. Note that the number of cell rearrangements, which can be estimated by following the variation of the number of neighbors for each cell, is significantly higher in simulations run with *pten* parameters, as observed in actual wings. This is due to the fluctuations in the simulations that can allow transient existence of unstable sides, thereby mimicking the fluctuations in actual wings. Last images correspond to Figures 4N'' and 4O'', respectively. (**A''',B'''**) Evolution of junction length heterogeneity. Last images correspond to Figures 4N''' and 4O''', respectively.

3 – Extended Experimental Procedures

Fly stocks

Stocks	References
<i>pten</i> ¹	Goberdhan et al., 1999
<i>pten</i> ¹¹⁷ , <i>akt</i> ¹ , <i>akt</i> ³	Stocker et al., 2002
<i>rok</i> ²	Winter et al., 2001
<i>baz</i> ^{Xi106}	Muller and Wieschaus, 1996
en-Gal4	Brand and Perrimon, 1993
tub-Gal80 ^{ts}	McGuire et al., 2003
hsflp; arm-GFP; act-FRT-Gal80-FRT-Gal4	gift of E. Martín-Blanco
UAS- <i>pten</i> ^{RNAi}	TRiP line #JF01859
UAS-dp110	Weinkove et al., 1999
Ubi-cadh-GFP	Oda and Tsukita, 2001
cadh-cadh-GFP	Huang et al., 2009
sqh-sqh-GFP	Royou et al., 2004
Ubi-Baz-Cherry	Bosveld et al., 2012
GRP1-GFP	Wartlick et al., 2011

Additional information can be found at FlyBase (<http://flybase.bio.indiana.edu/>).

Image treatments, quantification, intensity measurement and cell junction tracking.

Raw fluorescence images were denoised (Kervrann and Boulanger, 2006) to increase signal to noise ratio, except for quantification of signal intensity. Because wings tend to be tilted, images were projected using an automated Matlab program to project acquired *z*-stack of the wing tissue at the level of maximal apical E-Cad-GFP or Baz-Cherry signal (Bosveld et al., 2012). After projection, the different parts of the wing that have been filmed in different fields were stitched together using a customized version of the Fiji plug-in “Stitching”. After inter-image intensity equalization of these projected images, watershed was used to segment apical cell contours followed by extensive manual corrections. The different cell parameters (area, perimeter, number of neighbors,...) were measured from the resulting skeletons. Cell-cell junction lengths were measured by the distance between both vertices (chord length), and normalized by the average value of each tissue quantified, to enable comparison. 4-fold vertices are defined automatically by our segmentation program when a junction is below the resolution of the pixel (0.216 μm in our case). Statistical significance was assessed by χ^2 test between wt internal control and *pten* tissue. To determine the intensity of markers within a given cell junction *s*, we first determined the pixels making up junction *s* in skeletonized images, as well as all their nearest neighboring pixels and we defined I_s^{raw} as the mean fluorescence intensity calculated over these pixels. To be able to compare intensity heterogeneities of cells coming from different image parts or different images, we removed the background intensity I_i^{bg} . It was defined as the average over the pixels neighboring the skeletonized sides within a radius of 4 pixels around each

junction pixel, from which we removed the pixels used to calculate the side intensity I_s^{raw} . We defined side s intensity as $I_s = I_s^{\text{raw}} - I_i^{\text{bg}}$. We defined the heterogeneity of junction length within cell i , σ_i^l , as the standard deviation of cell i junction lengths, normalized by the average side length in cell i , $\langle l \rangle_i$:

$$\sigma_i^l = \frac{1}{\langle l \rangle_i} \left[\frac{1}{n_i} \sum_{s=1}^{n_i} (l_s - \langle l \rangle_i)^2 \right]^{1/2}$$

where l_s is side s chord length, and n_i is the number of cell i side lengths (or neighbors). Statistical significance was assessed by student t-test between wt internal control and *pten* tissue. Similarly, we defined the heterogeneity of side intensities within cell i , σ_i^I , as the standard deviation of cell i junction intensities, normalized by the average side intensity in cell i , $\langle I \rangle_i$:

$$\sigma_i^I = \frac{1}{\langle I \rangle_i} \left[\frac{1}{n_i} \sum_{s=1}^{n_i} (I_s - \langle I \rangle_i)^2 \right]^{1/2}$$

where I_s is the intensity of cell junction s .

Cell rearrangements were scored either manually or automatically. For manual tracking, skeletons were superimposed onto projected images of a time-lapse movie expressing E-cad-GFP (Movie S2A-B). Every junction on the first image was followed over time to manually count rearrangement events occurring to the successive junctions created between 4 (or more) cells. A new neighbor exchange was counted only when the program detected the creation of a new junction of 2 or more pixels, ignoring the 4-fold vertex if the junction regrew in the same direction as the old one. When quantifications were made in clones, only junctions created between cells of the same genotype were taken into account, excluding junctions at the boundary of the clone. For automated tracking a Matlab routine was developed. For each junction s analyzed, the relative intensity of Myo-GFP, Rok-GFP or GRP1:GFP was computed as the ratio between the junction intensity I_s^{raw} and the average intensity of the cell junctions lying in a square box of 40x40 pixels surrounding the junction of interest.

Numerical simulations

We used numerical simulations based on the cellular Potts model which is particularly relevant in biology to describe variable cell shape, size, packing and irregular fluctuating interfaces of cells (Glazier and Graner, 1993; Graner and Glazier, 1992; Kafer et al., 2007; Krieg et al., 2008; Marée et al., 2007; Mombach et al., 1995). Each cell is defined as a set of pixels, here on a 2D square lattice; their number defines cell area A . The pixelisation of the calculation lattice can be chosen to match the resolution of experimental images. A cell shape changes when one of its pixels is attributed to another cell instead.

We used periodic boundary conditions, with external medium surrounding cells (a state without adhesion or area and perimeter constraints). Our field of simulation was a rectangle of 325x475 pixels determined by the size of the loaded experimental images, then cropped to a rectangle of 285x403 to cut out external medium from displayed movies. Initially, the whole field was filled with cells because segmented experimental images come from parts of wing interveins. Then, at first simulation step, all cells touching the field borders were removed and replaced by external medium. Throughout the simulation, cell shapes were relaxed to decrease the energy E [eq. (1)].

The algorithm to minimize E uses Monte Carlo sampling and the Metropolis algorithm, as follows. We randomly draw (without replacement) a lattice pixel and one of its eight neighboring pixels. If both pixels belong to different cells, we try to copy the state of the neighboring pixel to the first one. If the copying decreases E , we accept it, and if it increases E , we accept it with probability $P = \exp(-\Delta E/T)$, where $\Delta E = E_{\text{after}} - E_{\text{before}}$. The prefactor T is a fluctuation (random copying) allowance; it determines the extent of energy-increasing copy events, leading to membrane fluctuations (Kafer et al., 2007; Mombach et al., 1995). Because all energy parameters are scalable with T , we can fix it without loss of generality; for numerical convenience, we choose numbers on the order of 10^3 . We define one Monte Carlo time step (MCS) as the number of random drawings equal to the number of lattice pixels. These simulations enable to find a state of mechanical equilibrium of a group of cells that relaxes from an initial configuration of higher energy (they do not necessarily accurately describe the actual tissue dynamics leading to this equilibrium state).

We ran simulations during 3000 MCS to reach a shape that no longer evolves, that is, in mechanical equilibrium where stresses are balanced. To better explore the energy landscape, simulations were run at $T=10^4$ for 2000 MCS, then annealing was performed during 750 MCS, linearly decreasing T down to $T = 2 \cdot 10^3$. To avoid possible effects of lattice anisotropy on cell shapes, we computed P and ΔE by including interactions up to the 20 next-nearest neighbors (Holm et al., 1991; Kafer et al., 2007). All perimeters indicated here were corrected by a suitable prefactor 11.3 to ensure that a circle with an area of A pixels has a perimeter $2\sqrt{\pi A}$ (Kafer et al., 2007). Except for Λ values that are different in *wt* and *pten*, all simulations were run using the same other parameters that follow: $A_o = 400, K = 1, X = 10$ [eq. (1)]. Λ values were calculated from dimensionless λ_{ij} value using its definition $\Lambda_{ij} = -2KA_o^{1/2}\lambda_{ij}$. For any cell i in contact with the medium for both *wt* and *pten*, we used $\lambda_{\text{medium},i} = -1$, thus making the interaction cell-medium very unfavorable and preventing the presence of medium between cells. For neighboring cells ij , we used the values determined from data fit of laser ablation experiments (Figure S2D-E), namely $\lambda_{ij} = \lambda_o = 2.3$ for *wt*; $\lambda_{ij} = \lambda_s = 1.8$ and $\lambda_{ij} = \lambda_L = 2.9$ for *pten*.

Analysis of temporal correlation between MyosinII-GFP intensity and junction length.

To study the correlation between MyoII-GFP intensity and junction length, we filmed a wt wing expressing MyoII-GFP at high temporal resolution (12 frames min^{-1}), during 10 minutes. We then picked 8 junctions that displayed significant changes of length during this period. For each junction and at each time point, we scored its vertex-to-vertex length and its intensity in MyoII-GFP (intensity averaged over all pixels of the junction). To be able to compare junction length with MyoII intensity, we renormalized each signal by its mean over the movie duration and subtracted its mean, therefore yielding dimensionless quantities with zero average (gray and green curves in Figure 3J). Because short junctions are associated with high MyoII intensity (anti-correlation), we flipped the MyoII signal (symmetry with respect to the time axis) to make easier the study of MyoII-length correlation.

To study this correlation we defined a function M that introduces a time delay τ between two functions and calculates the area between their curves (Figure S3N). Thus, for any functions $F(t)$ and $G(t)$ defined on $[0, T_{\max}]$, we define the delay function $M(\tau)$ as:

$$M(\tau) = 1 - \frac{\int_{-T_{\max}}^{2T_{\max}} dt |\tilde{F}(t) - \tilde{G}(t + \tau)|}{\int_0^{T_{\max}} dt (|F(t)| + |G(t)|)}$$

with τ in $[-T_{\max}, T_{\max}]$ ¹. Here the denominator ensures that $M(\tau)$ reaches 0 on the domain boundaries when $F(t)$ and $G(t + \tau)$ do not overlap at all. This function is more robust to the noise than the classical correlation function using the product $F(t)G(t + \tau)$ (not shown). M verifies $0 < M(\tau) < 1$ and reaches a maximum M^* when the area between $F(t)$ and $G(t + \tau)$ is minimal, namely for the time delay τ^* corresponding to the best match between the variations of the two curves (Fig. S3N').

For each junction analyzed, we used M to determine the time delay corresponding to the best match between junction length (L) and flipped MyoII intensity (Fig. 3K). Because both L and MyoII are noisy, $M(\tau)$ was smoothed by averaging over a sliding window of 5 time points to make the determination of its maximum M^* and the corresponding time delay τ^* more robust to noise.

To assess the L -MyoII temporal correlation, we studied the best match between two uncorrelated functions taking random values in the domains $[-0.38, 0.38]$ and $[-0.26, 0.26]$ that correspond to the

¹Note that $t + \tau$ belongs to $[-T_{\max}, 2T_{\max}]$ and definitions of functions F and G must be extended to this domain. Calling \tilde{F} and \tilde{G} their extensions:

$$\tilde{F}(t) = \begin{cases} F(t), & t \text{ in } [0, T_{\max}] \\ 0, & \text{elsewhere} \end{cases} \quad \tilde{G}(t + \tau) = \begin{cases} G(t + \tau), & t \text{ in } [-\tau, -\tau + T_{\max}] \\ 0, & \text{elsewhere} \end{cases}$$

average variations of dimensionless length and MyoII intensity measured in our 8 experiments, respectively (Fig. S3O). In such cases, $M(\tau)$ does not display noticeable peaks resulting in large variations of τ^* values (Fig. S3O'). The analysis of 1000 simulated couples of such uncorrelated functions yielded an average $\langle \tau^* \rangle = -1 \pm 24$ s, with strong variations around the mean, as expected (Fig. S3O'). As for M maxima, we found $\langle M^* \rangle = 0.32 \pm 0.01$. We used this result to define the time correlation threshold $M_{\text{rand}} = 0.33$, and considered that for $M^* < M_{\text{rand}}$, two functions were not correlated (dashed red lines in Fig. 3K, S3N', O').

Because some of the MyoII(t) and $L(t)$ curves displayed some repeated patterns, on each analyzed junction, we performed an auto-analysis of both length and MyoII curves in order to avoid the determination of time delays corresponding to correlations with a wrong pattern. The smallest value obtained was 85s, and in the following we therefore only considered the maxima of M corresponding to a time delay τ in the range $[-85\text{s}, 85\text{s}]$.

Applying the correlation criterion ($M^* > M_{\text{rand}}$), we found that 7 out of the 8 analyzed junctions displayed a correlation between L and MyoII (one shown in Fig. 3J). We calculated the average time delay over these 7 junctions and found $\langle \tau^* \rangle = -9 \pm 7$ s, that is significantly negative ($p=0.01$, one sample left-tailed t-test) (Fig. 3K). Note that we found $\tau^* < 0$ for 6 out these 7 junctions, the only positive value being $\tau^* = 0.5$ s.

Finally, to assess the influence of the smoothing of M and the robustness our time delay determination, we changed the number of points used for smoothing M from 5 to 1, 3, and 7. Averaging the $\langle \tau^* \rangle$ values obtained in these different cases, we found $\langle \langle \tau^* \rangle \rangle_{\text{smooth}} = -9 \pm 1$ s, where the standard deviation of 1s reflects the weak sensitivity of our method to the choice of smoothing that leaves the results unchanged.

Quantitative analysis of wing morphogenesis.

To characterize tissue shape changes in the wing, as well as the underlying cell dynamics in term of cell shape changes and cell rearrangements, we applied a multi-scale formalism that has been validated on foam dynamics (Graner et al., 2008), and that we generalized more recently to study the morphogenesis of living tissues (Bosveld et al., 2012, Figure 5A-A''). This formalism is based on a matrix called the ‘‘texture’’ that is built with the links connecting each cell center to the centers of its neighbors. The texture of a single cell i reads:

$$M_i = \frac{1}{2} \sum_j \omega_{ij} m_{ij}$$

where j labels each neighbor of cell i , the vector $\vec{l}_{ij} = (X_{ij}, Y_{ij})$ is the link between the centers of cells i and j , the factor $1/2$ avoids counting twice each link, the weight ω_{ij} is 1 for all normal links and $1/2$ for the few links belonging to a 4-fold vertex, and m_{ij} is the tensor (or outer) product of \vec{l}_{ij} by itself:

$$m_{ij} = \vec{l}_{ij} \otimes \vec{l}_{ij} = \begin{pmatrix} X_{ij}^2 & X_{ij}Y_{ij} \\ Y_{ij}X_{ij} & Y_{ij}^2 \end{pmatrix}$$

By storing the information of link lengths and angles for each cell, the texture characterizes cell size and the amplitude and direction of its anisotropy, namely its shape, and is expressed in μm^2 (Graner et al., 2008, Bosveld et al., 2012). Now considering a box delimiting a part of the tissue and the group of cells having their centers within this box at time t , the total texture M of this group of cells reads (eq. 6 of ref. Graner et al., 2008):

$$M(t) = \sum_i M_i(t) = \sum_i \frac{1}{2} \sum_j \omega_{ij} m_{ij}$$

The cumulative variation of texture over the time period of measurements T in this box is $\Delta M = M(t+T) - M(t)$. Cell shape changes in the box are characterized by the rate of texture variation, $\Delta M/T$, and expressed in $\mu\text{m}^2 \text{min}^{-1}$ (Figure 5A, eq. C3 in ref. Graner et al., 2008). Cell shape changes are thus measured as matrices, in order to retain information regarding their direction and anisotropy, which is relevant to characterize contributions to tissue shape changes. In what follows we do not use their trace that is related to changes in cell sizes. Cell shape changes are represented as cyan bars along the direction of cell contractions (Figure 5A-A’’).

Cell rearrangements were also directly measured as matrices in the same formalism and expressed in the same units, namely $\mu\text{m}^2 \text{min}^{-1}$ (eq. 11 of ref. Graner et al., 2008). They quantify the topological changes in the plane of the epithelium. (Figure 5A’) At time t , we listed cells i having their centers in the box in two successive images $t, t+\delta t$ and that did not divide during δt . The total cell rearrangement rate of these cells was measured as $R(T)/T$ where $R(T)$ was the sum of cell rearrangements at each time interval δt , defined as follows:

$$R(\delta t) = -\sum_i \frac{1}{2} \left(-\sum_{j_l} \omega_{ij_l} m_{ij_l} + \sum_{j_g} \omega_{ij_g} m_{ij_g} \right)$$

Here the sums are taken on links ij_l which are *lost* during δt , i.e. cells which were neighbors of i at t but no longer at $t + \delta t$: they contribute negatively. Similarly, links ij_g which are *gained* during δt , that is, cells which become neighbors of i at $t + \delta t$ contribute positively. They are represented as red bars along the direction of gained center-center links, thus in the direction of new neighbors or lost cell-cell junctions (Figure 5A-A’’). This direction corresponds to a local contraction of the tissue (Figure 5A’). It is important to note that if two cells transiently lose their junction, then regain it, their link disappears then re-appears, and the total contribution of such back-and-forth rearrangements to the cell

rearrangement matrix R is close to zero, as it should be. When a four-fold vertex was detected during a rearrangement, the corresponding links were counted with a weight $\omega=1/2$ so that the total contribution of the corresponding cell rearrangement was independent of the detection or definition of a four-fold vertex.

Tissue shape changes are given by cell geometrical changes (Graner et al., 2008; Marmottant et al., 2008) and were also directly measured as matrices in the same formalism and the same units ($\mu\text{m}^2 \text{min}^{-1}$) (eq. 10 of ref. Graner et al., 2008). At time t , we listed cells i having their centers in the box in two successive images $t, t+\delta t$ and that did not divide during δt . The total rate of geometric changes of these cells was measured as $B(T)/T$ where $B(T)$ was the sum of geometrical changes at each time interval δt , defined as follows:

$$B(\delta t) = \sum_i \frac{1}{2} \sum_{j_c} \omega_{ij_c} \delta m_{ij_c} \quad \text{with} \quad \delta m_{ij_c} = m_{ij_c}(t + \delta t) - m_{ij_c}(t)$$

Here the sums are taken on links j_c which are *conserved* during δt , i.e. cells that were neighbors of i both at t and at $t + \delta t$. They are represented as blue bars along the direction of tissue contraction (Figure 5A-A’). When tissue shape changes mostly occur through cell rearrangements and cell shape changes with negligible contributions of divisions, apoptoses or flux of cells, the balance on links yields (Graner et al., 2008):

$$B \approx \Delta M + R$$

which is relevant to our study of morphogenesis in the wing between 24 and 29 hAPF. Thus, figure 5A-a’ illustrate how the tissue can achieve the same contraction-extension by pure cell shape changes (5A), or by pure cell rearrangements (5A’), or how these two processes can cancel out to result in no local change of tissue shape (5A’).

We applied this formalism to study the morphogenesis of the wing and the influence of *pten* loss of function. We segmented 2 wt and 2 *pten* movies and performed our quantitative analysis on each movie in the time-interval 24-29 hAPF. Movies were realigned with respect to the L3 vein. The analyzed regions were defined by 3 identical square boxes ($54 \times 54 \mu\text{m}^2$) spanning the intervein width and located at $d=40 \mu\text{m}$ from the posterior cross vein (Figure 5B). The registration in time and space of the different movies enabled to define the ensemble average over N movies of the wing of a quantity Q calculated in the box b at time t and for the genotype g , thus providing a better signal to noise ratio (Bosveld et al., 2012):

$$Q_g(b, t) = \frac{1}{N} \sum_n^N Q_g(b, t, n)$$

Q can be B , R or ΔM . This also enables the definition of its standard deviation δQ_g . Our level of detection at time t , $\varepsilon Q_g(t)$, can be estimated by taking the average of $\delta Q_g(b, t)$ over the locations b and over each components:

$$\varepsilon Q_g(t) = \frac{1}{3} \left(\langle \delta Q_g^{xx}(t) \rangle_b + \langle \delta Q_g^{xy}(t) \rangle_b + \langle \delta Q_g^{yy}(t) \rangle_b \right)$$

Since $\varepsilon Q_g(t)$ reflects our detection level, $Q_g(b,t)$ was considered as significant if $|\lambda_{Q_g}|(b,t)$, positive eigenvalue of $Q_g(b,t)$, was larger than $\varepsilon Q_g(t)$ and plotted as a color bar, or as a gray bar in the opposite case ($|\lambda_{Q_g}|(b,t) < \varepsilon Q_g(t)$) (Bosveld et al., 2012, Figure 5C).

This also enabled us to use our subtractive method (Bosveld et al., 2012) and calculate the local differences in cell rearrangements, cell shape changes and tissue contraction-extension in wt and mutant conditions, (red, cyan and blue bars in Figure 5C, respectively). This led to the determination of the specific contribution of PTEN to each of these processes (Figure 5C).

Quantitative analysis of PCP organization in the wing.

Characterization of planar cell polarity (PCP) in wt and *pten* wings was performed by analyzing the distribution of Strabismus (Stbm) intensity around the cortex of cells making up the wing interveins. To achieve this, we segmented 3 wt and 3 *pten* wings and scored the intensity of Stbm-YFP of each pixel around each segmented cells. At our resolution (0.2 $\mu\text{m}/\text{pixel}$), a width of 3 pixel along each segmented junction was sufficient to capture all the pixels displaying Stbm intensity at each junction without significantly brimming over the inside/outside of cells. To minimize the impact of intensity fluctuations in the image, the local background intensity was calculated around each junction over a width of 13 pixels along each junction (after having previously excluded the pixels corresponding to Stbm intensity) and subtracted from the intensity value at each pixel around each cell. At this point, we had for each cell the list of pixels of its extended contour (3-pixel width) and a value of the intensity (without background) at each of these pixels.

To quantify the distribution of Stbm intensity around each cell cortex and across the wing, we developed an original approach based on the determination of the first two Fourier modes of the intensity around each cell cortex. Calling $I(\theta)$ the Stbm intensity at the cell cortex at the angle θ , we calculated:

$$A_0 = \frac{1}{2\pi} \int_{-\pi}^{\pi} d\theta I(\theta) \quad ; \quad A_n = \frac{1}{\pi} \int_{-\pi}^{\pi} d\theta I(\theta) \cos(n\theta), \quad B_n = \frac{1}{\pi} \int_{-\pi}^{\pi} d\theta I(\theta) \sin(n\theta), \quad 1 \leq n \leq 2$$

The 0th mode gives the mean intensity around the cortex, the 1st mode can be represented by a vector pointing in a direction of strong intensity around the cortex, the 2nd mode can be represented by a tensor indicating an axis of strong intensity around the cell cortex and is particularly relevant to characterize PCP in a planar tissue. Practically, to calculate the modes A_n, B_n , we divided each cell in 18 equal angular domains of 20°. Then we calculated the mean intensity of the contour pixels in each domain, thereby enabling the calculation of the integrals giving A_n, B_n . We found that in the wing the

1st mode of Stbm intensity was always much weaker than the two others. One can therefore approximate:

$$I(\theta) \approx A_0 + A_2 \cos 2\theta + B_2 \sin 2\theta = I_0 + I_2 \cos 2(\theta - \varphi_2)$$

where we have introduced the Fourier modes in polar coordinates: $A_0 = I_0$, $A_2 = I_2 \cos 2\varphi_2$ and $B_2 = I_2 \sin 2\varphi_2$. To easily characterize the Stbm distribution in the wing, we built a symmetric fluorescence tensor F that contains the all information on the 0th and 2nd modes:

$$F = \frac{1}{2} \begin{pmatrix} A_0 + A_2 & B_2 \\ B_2 & A_0 - A_2 \end{pmatrix} \quad \tilde{F} = \frac{1}{2} \begin{pmatrix} I_0 + I_2 & 0 \\ 0 & I_0 - I_2 \end{pmatrix}$$

where \tilde{F} is the diagonalized version of F . $\text{Tr}(F) = A_0$ gives the average intensity. We can extract from F a traceless polarity tensor P that only depends on the 2nd Fourier mode:

$$P = F - \frac{\text{Tr}(F)}{2} I_d = \frac{1}{2} \begin{pmatrix} A_2 & B_2 \\ B_2 & -A_2 \end{pmatrix} \quad \tilde{P} = \frac{1}{2} \begin{pmatrix} I_2 & 0 \\ 0 & -I_2 \end{pmatrix}$$

We used P (\tilde{P} , once diagonalized) to identify and characterize a putative axis of strong intensity around the cell cortex by quantifying its amplitude and direction, which can be represented by a bar of length I_2 and making the angle φ_2 with the x axis (Figure 5E-G). This approach is therefore particularly relevant to characterize PCP in a planar tissue (Figure 5E-G). In the same way that we previously only considered the traceless parts of cell rearrangements (R), cell shape changes (ΔM) and tissue shape changes (B), we only considered P to characterize wing morphogenesis in this work. By having defined such a polarity tensor, we could therefore use the same powerful methods we used to characterize morphogenesis in the wing and perform the same operations: sums, averages over cells, over wings and subtractions (Figure 5H)

Theoretical Model of Ordered Cellular Packing

In this part, we briefly present the main results of the model we used and justify the assumptions we made. The periodic lattice description we use hereafter does not aim at describing the wing intervein as a whole, but more at understanding some of the ordered cellular patterns that can be observed at different locations in wing interveins, namely the honeycomb-like patterns observed in wt cell patches, and most interestingly, the cobblestone patterns in *pten* mutant tissue (in orange in Figure 1B).

1) Theoretical Model of Cellular Packing

1.1) General Model: energy of cellular packing and side tension

To make this supplemental text easier to read, we re-derive in this subsection some results from published material using our own framework, pointing out what is most relevant to our study.

Several epithelial cell packings in *Drosophila* embryo, pupal wing and retina have been successfully described by minimizing an energy that balances adhesion between cells and cortex contractility

(Aigouy et al., 2010; Farhadifar et al., 2007; Graner and Sawada, 1993; Kafer et al., 2007; Ouchi et al., 2003; Rauzi et al., 2008; Staple et al., 2010):

$$(1) \quad E = \sum_{\text{sides } ij} \Lambda_{ij} L_{ij} + \sum_{\text{cells } i} \left[\frac{1}{2} K_i P_i^2 + \frac{1}{2} X_i (A_i - A_i^o)^2 \right]$$

The energy E includes two types of quantities: (i) *geometrical variables*: A_i is the apical area of cell i ($i=1$ to N , N being the total number of cells), P_i its apical perimeter, and L_{ij} the length of the apical side ij that separates cell i and cell j ; (ii) *physical parameters*: K_i , A_i^o and X_i are all *cell specific* quantities; they model the cortical rigidity due to cell i acto-myosin cortex ring at cell apical surface, cell i preferred area, and the elastic modulus ensuring volume conservation of cell i , respectively. Λ_{ij} is the *side specific* line energy due to competition between adhesion (cadherins) and cortex contractility (acto-myosin) at side ij (Lecuit and Lenne, 2007). The energy E thus contains two terms in competition: (i) a linear term that tends to increase side length L_{ij} provided that $\Lambda_{ij} < 0$, which is always verified in what follows (discussed in section 1.2); (ii) a quadratic term that tends to minimize perimeter P_i by rounding up cell i , and therefore tends to decrease the total contact length between cell i and its neighbors. The area term $\frac{1}{2} X_i (A_i - A_i^o)^2$ ensures that area A_i remains close to the target area A_i^o .

Cells are assumed to be surrounded by a medium (that we consider as cell # 0 for convenience) that has no area or perimeter constraints, namely $K_0 = 0$ and $X_0 = 0$. With such a surrounding medium, periodic boundary conditions are trivially satisfied, and cell i perimeter is the sum of sides shared with cells j neighboring cell i and reads:

$$(2) \quad P_i = \sum_{\langle j \rangle} L_{ij}$$

Under the assumption that the adopted cellular pattern corresponds to a minimum of energy E , which has been shown to be relevant to several different epithelial tissues (Aigouy et al., 2010; Farhadifar et al., 2007; Hilgenfeldt et al., 2008; Kafer et al., 2007; Rauzi et al., 2008; Staple et al., 2010), the actual *line tension* (or *interfacial tension*) T_{ij} of side ij can be derived from the energy E and reads:

$$(3) \quad T_{ij} = \frac{\partial E}{\partial L_{ij}} = \Lambda_{ij} + K_i P_i + K_j P_j$$

where $\partial / \partial L_{ij}$ denotes derivation with respect to L_{ij} while keeping all areas and all other side lengths constant. Note that perimeters P_i and P_j must vary through such a transformation, and therefore both contribute to $\partial E / \partial L_{ij}$ in eq. (3). Accordingly, the actual line tension T_{ij} of side ij is not solely due to line energy Λ_{ij} , but also involves the cortical elastic contributions of both cells sharing this side.

Line tension T_{ij} is a measurable model-independent physical quantity. The force balance at each vertex v implies that line tensions of all sides meeting at this vertex cancel out: $\sum_v \vec{T} = 0$. Therefore, possible line tension differences among sides that meet at vertices (referred to as *heterogeneity* of line tension hereafter) may have consequences on cellular arrangements. So far such consequences have been studied in the context of cell mixing involving a specific line tension at the interface of two cell populations (Landsberg et al., 2009), in cell elongation and orientation of divisions (Mao et al., 2011), or as a mechanism driving cell intercalation (Rauzi et al., 2008). Here, we study the domain of existence and stability of the configurations of a cellular lattice with identical or different side lengths as we observe in wt and *pten* mutant tissues.

The formalism presented here is general and can be significantly simplified to its essential ingredients required to capture the effect of heterogeneity of side physical properties on cell packing, and figure out whether it can account for the cobblestone patterns observed in *pten* tissue.

1.2) Model simplification and side parameter λ

Observation of wing intervein tissues show that they are made up by a single population of cells (similar aspect and apical size at the end of wing morphogenesis ~ 30 hAPF, Figure 1A). We therefore assume that cells have same *cellular* properties, namely $K_i = K$, $X_i = X$ and $A_i^0 = A_o$, which is commonly made (Farhadifar et al., 2007; Kafer et al., 2007; Staple et al., 2010). Moreover, because at this time of development we do not observe major differences in cell areas neither between cells from the same tissue (and consistently, no significant curvature of their sides), nor between cells from wt and *pten* tissues, we assume that cell adopt and keep their target area, namely that $A_i = A_o$, as done in refs. (Gemp et al., 2011; Hilgenfeldt et al., 2008; Rauzi et al., 2008). Accordingly, we drop the area term in eq. (1). A_o can be estimated from actual tissues by $A_o = \langle A \rangle$.

We now use cell target area A_o and cortical rigidity K to define dimensionless quantities independent of average cell size: the average energy per cell $e = E / 2NKA_o$, perimeters $p_i = P_i / A_o^{1/2}$, lengths $l_{ij} = L_{ij} / A_o^{1/2}$, line tensions $\gamma_{ij} = T_{ij} / 2KA_o^{1/2}$, and most importantly, the ratios between line energy and cortical rigidity at each side ij , that we call the “side parameters” λ_{ij} which reads:

$$(4) \quad \lambda_{ij} = \frac{-\Lambda_{ij}}{2KA_o^{1/2}}$$

Note the minus sign in eq. (4) so that λ_{ij} is positive when existence of side ij is favored ($\Lambda_{ij} < 0$). The side parameter λ_{ij} increases with adhesion (i.e. increasing $|\Lambda_{ij}|$), decreases with side specific contractility (i.e. decreasing $|\Lambda_{ij}|$), and decreases with cell cortical rigidity (i.e. increasing K).

Importantly, λ_{ij} does not depend on side length l_{ij} . The dimensionless line tension at side ij reads [eqs. (3) and (4)]:

$$(5) \quad \gamma_{ij} = \frac{1}{2}(p_i + p_j) - \lambda_{ij}$$

At the cell-medium interface, eq. (5) becomes: $\gamma_{0i} = \frac{1}{2}p_i - \lambda_{0i}$. The average dimensionless energy per cell e simplifies to:

$$(6) \quad e = \frac{1}{N} \sum_{\text{cells } i} \left[\frac{1}{4} p_i^2 - \sum_{\langle j \rangle} \frac{1}{2} \lambda_{ij} l_{ij} \right]$$

The side parameters λ_{ij} are the key parameters of the model: they represent the competition between adhesion and cortical contractility at each side ij , and both their sign and relative amplitude matter. In the following we only consider cases $\lambda_{ij} \geq 0$ that favor the existence of all apical contact between cells. Finally, we take $\lambda_{ij} \leq p_H$, where $p_H = 2^{3/2}3^{1/4} \approx 3.72$ is the normalized perimeter of the regular hexagon, which ensures that line tension remains positive in all sides. Indeed, since the regular hexagon is the shape with smallest dimensionless perimeter p_H that tiles the plane (Hales, 2001), any cell shape of a periodic lattice verifies $p_i \geq p_H$: using eq. (5) one gets $\gamma_{ij} \geq p_H - \lambda_k \geq 0$. These two limits define the relevant physical range of side parameter values of our study:

$$(7) \quad 0 \leq \lambda_{ij} \leq p_H$$

Finally, in addition to displaying similar areas in wing intervein, groups of cells can also display very similar shapes (in orange in Figure 1B). To better understand how these local cobblestone shaped patterns can arise in these clusters, we now consider periodic lattices made by identical six-sided cells of perimeter p , but whose sides can nevertheless have different properties (Figure 2A inset). This makes the model analytically tractable. Such an ordered lattice can then only have three types of sides, each type having its specific line parameters $\lambda, \lambda_\alpha, \lambda_\epsilon$, line tensions $\gamma, \gamma_\alpha, \gamma_\epsilon$, and lengths l, l_α, l_ϵ , respectively (blue, green, red in Figure 2A inset). The energy e now becomes the actual energy per cell and reads:

$$(8) \quad e = \frac{1}{4} p^2 - (\lambda l + \lambda_\alpha l_\alpha + \lambda_\epsilon l_\epsilon)$$

Taking the ‘‘blue’’ side as reference and introducing the length ratios $\alpha = l_\alpha / l$ and $\epsilon = l_\epsilon / l$, line tensions γ_k , side parameters λ_k , and cell perimeter p read:

$$(9) \quad \gamma_k = \frac{\partial e}{\partial l_k} = p - \lambda_k \quad \lambda_k = \frac{-\Lambda_k}{2KA_o^{1/2}} \quad p = 2(1 + \alpha + \epsilon)l$$

Using this expression of p , l can be eliminated from eq. (8) in e :

$$(10) \quad e = \frac{p}{2} \left(\frac{p}{2} - \langle \lambda \rangle \right) \quad \text{with} \quad \langle \lambda \rangle = \frac{\lambda + \alpha \lambda_\alpha + \epsilon \lambda_\epsilon}{1 + \alpha + \epsilon}$$

where $\langle \lambda \rangle$ is the average of the three side parameters weighted by their lengths. For what follows, it is convenient to subtract the energy of the honeycomb configuration e_H corresponding to $\alpha = \varepsilon = 1$ and $p = p_H$ with the same set of side parameters $(\lambda, \lambda_\alpha, \lambda_\varepsilon)$, and define the energy difference:

$$(11) \quad \Delta e = e - e_H \quad \text{with} \quad e_H = \frac{p_H}{2} \left(\frac{p_H}{2} - \frac{\lambda + \lambda_\alpha + \lambda_\varepsilon}{3} \right)$$

that represents the energy gain of adopting the cellular arrangement corresponding to the energy minimum associated to side parameters $(\lambda, \lambda_\alpha, \lambda_\varepsilon)$ instead of the honeycomb pattern.

2) Model predictions I: two alternative hypotheses for cobblestone patterns

To determine the cellular configurations corresponding to a given set of side parameters $(\lambda, \lambda_\alpha, \lambda_\varepsilon)$, we use the force balance at each vertex, the area constraint, and achieve numerically the determination of the minima of energy e (or equivalently Δe) with respect to (α, ε) (top of Figure S2A-C).

2.1) Homogeneous limit: same side properties ($\lambda = \lambda_\alpha = \lambda_\varepsilon = \lambda_o$)

In the simplest case where sides all have same physical properties, i.e. same side parameter value: $\lambda = \lambda_\alpha = \lambda_\varepsilon = \lambda_o$, all sides have same line tension $\gamma_o = p - \lambda_o$ [eq. (9)]. In this limit, one can show that there are two cases to consider according to λ_o values, whether it is greater or smaller than $p_H = 2^{3/2}3^{1/4} \approx 3.72$, the dimensionless perimeter of a regular hexagon.

- *Low* side parameter: $0 < \lambda_o < p_H$

The energy landscape displays a single minimum for $\alpha = \varepsilon = 1$ (Figure S2A top) and the cellular network adopts a honeycomb pattern similar to the cellular arrangement observed in wt tissue (Figure 2A, S2A bottom). Perimeter reaches value $p = p_H$ and sides are under positive line tension [eq. (9)]:

$$(12) \quad \gamma_H = p_H - \lambda_o > 0$$

- *High* side parameter: $\lambda_o > p_H$

Even though λ_o then lies outside our range of study [eq. (7)] it is worth considering this case in this homogeneous limit. The energy landscape drastically changes for $\lambda_o > p_H$ since the honeycomb pattern corresponding to $\alpha = \varepsilon = 1$ now becomes a local maximum of the energy and is surrounded by a valley of equivalent energy minima (Figure S2B top). All network configurations corresponding to these minima differ by the values taken by the geometrical parameters $(l, l_\alpha, l_\varepsilon, \omega, \theta)$ but they all share the same energy and are therefore degenerate. Two equivalent configurations are represented in bottoms of Figures S2B and S2C. Interestingly, for $\lambda_o \approx 4$, cellular networks can adopt cobblestone configurations, very similar to local patterns observed in *pten* tissue (Figure 2C, S2C case 1). One can

show that all these configurations are characterized by the same perimeter $p = \lambda_o$, and a vanishing side tension in every side [eq. (9)]:

$$(13) \quad \gamma_o = p - \lambda_o = 0$$

- Transition honeycomb-soft cobblestone

By increasing the side parameter λ_o from $\lambda_o < p_H$ to $\lambda_o > p_H$, it is therefore possible to go from a tensed honeycomb pattern to a soft cobblestone patterns while having homogeneous side parameters (“homogeneous and $\gamma=0$ ” hypothesis). A variation of λ_o represents a displacement of the balance between cell adhesion and cortical rigidity: an increase of adhesion $|\Lambda|$, or equivalently, a decrease of cortical rigidity K will both increase λ_o . Therefore, these results suggest that the breaking of side length symmetry in *pten* tissue could either be due to a homogeneous increase of adhesion at all sides, or equivalently, to a decrease of cell cortical rigidity.

2.2) General case: heterogeneity of side properties ($\lambda \neq \lambda_\alpha \neq \lambda_\epsilon$)

Alternatively, the breaking of side length symmetry in *pten* wings may as well be a direct consequence of heterogeneity of side properties within cells, i.e. different side parameter values for each type of side: $\lambda \neq \lambda_\alpha \neq \lambda_\epsilon$. For λ_k values in our range of study [eq. (7)], the energy landscape displays a single minimum that does not correspond to a honeycomb packing [$(\alpha, \epsilon) \neq (1, 1)$, Figure S2C top]. Under these assumptions we also found network arrangements displaying cobblestone configurations similar to parts of *pten* tissue (case 2 in Figures 2B, S2C).

These patterns can look exactly similar to the one obtained in the homogeneous case (case 1 in Figures 2B, S2C). However, it is important to note that they are fundamentally different for three reasons: (i) the cellular network is under tension: the three types of sides experience strictly positive line tensions γ_k ; (ii) each triplet of side heterogeneity $(\lambda, \lambda_\alpha, \lambda_\epsilon)$ has a unique minimum of energy e and corresponds to a unique cellular pattern; (iii) the side length heterogeneity directly comes from heterogeneous side parameter values and is not a spontaneous symmetry breaking. We refer to this case as the “heterogeneous and $\gamma > 0$ ” hypothesis.

Moreover, in such cobblestone patterns arising from heterogeneity of cell side parameters, the model predicts a decrease of the relative side length l with increasing line tension γ . Indeed, for a given cellular network characterized by the triplet (Figure S2C):

$$(14) \quad \lambda > \lambda_\alpha > \lambda_\epsilon \Rightarrow \begin{cases} \gamma < \gamma_\alpha < \gamma_\epsilon \\ l > l_\alpha > l_\epsilon \end{cases}$$

The explicit relationship $l = f(\gamma)$ cannot be obtained analytically in the general case, i.e. for any triplet $(\lambda, \lambda_\alpha, \lambda_\epsilon)$, because the determination of the energy minimum, and corresponding length $(l, l_\alpha, l_\epsilon)$ and angles (ω, θ) , is achieved numerically. From eq. (14), one can expect a negative correlation when plotting γ vs. l .

This relationship can nevertheless be obtained analytically for cellular lattices featuring weak heterogeneity of side parameters (honeycomb-like packing), by performing a linear expansion in the vicinity of the homogeneous case corresponding to the honeycomb pattern:

$$\lambda_k = \lambda_o + \delta_k \quad \text{with} \quad \delta_k \ll \lambda_o < p_H$$

Assuming that the side parameters $(\lambda, \lambda_\alpha, \lambda_\epsilon)$ are evenly distributed around λ_o with same dispersion σ_λ , namely that $\langle \delta_k \rangle = 0$ and $\langle \delta_k^2 \rangle = \sigma_\lambda^2$, one can show that the mean and dispersion of side length l_k in the lattice at equilibrium are given by:

$$(15) \quad \langle l_k \rangle \approx -\frac{p_H}{3\gamma_H} \gamma_k + \frac{p_H}{2} \quad \text{and} \quad \sigma_{l_k} \approx \frac{p_H}{3\sqrt{2}} \frac{\sigma_\lambda}{\gamma_H}$$

where averages have been taken over sides $m, n \neq k$, and where second order terms in δ^2 have been neglected. Eq. (15) explicitly shows the negative correlation between l and γ , namely the higher the tension, the shorter the side.

2.3) Conclusion and comparison with laser ablation experiments

These results show that cobblestone arrangements similar to local ordered patterns observed in *pten* cell patches (Figure 1B) can also results from heterogeneity of side physical properties (“heterogeneous and $\gamma > 0$ ” case) (Figure 2B, S2C). This heterogeneity entails that side tension is strictly positive in all sides, and decreases with increasing side length.

As explained in the main text, our experiments of laser ablation of single junctions helped us rule out the “homogeneous and $\gamma = 0$ ” hypothesis and validate the “heterogeneous and $\gamma > 0$ ” hypothesis. Indeed, the tension T_{ij} of the cell junction ij can be determined up to an unknown prefactor by laser ablations of side ij and measurement of the initial relaxation velocity of its vertices V_{ij}^o (Farhadifar et al., 2007; Hutson and Ma, 2007; Hutson et al., 2009; Landsberg et al., 2009; Rauzi et al., 2008):

$$(16) \quad V_{ij}^o = \mu T_{ij}$$

where μ is an unknown prefactor having the dimensions of the inverse of a friction coefficient.

3) Inference of side parameter values from laser ablation experiments

3.1) Principle

We then decided to estimate quantitatively cell side heterogeneity in wt and *pten* tissues, by probing the relationship between cell perimeters and initial relaxation velocities in our experimental data. Indeed, eq. (5) links dimensionless line tension γ_{ij} , perimeter sum $p_i + p_j$, and side parameter λ_{ij} . Using initial relaxation rate $v_{ij}^o = V_{ij}^o / 2\langle A \rangle^{1/2}$ (expressed in s^{-1}) and characteristic time $\tau = 1/\mu K$ (s), we rewrite eq. (16) as $\gamma_{ij} = \tau v_{ij}^o$, and inject it in eq. (5), which leads to:

$$(17) \quad \frac{1}{2}(p_i + p_j) = \tau v_{ij}^o + \lambda_{ij}$$

Therefore, when plotting the sum of dimensionless perimeters $\frac{1}{2}(p_i + p_j)$ vs. relaxation rate v_{ij}^o , eq. (17) predicts points distributed along an ascending straight line of slope $\tau > 0$ and of zero-intercept λ_{ij} with dispersion due to biologic variability and measurement errors. Thus, the model side parameters $(\lambda, \lambda_\alpha, \lambda_\epsilon)$ can, in principle, be directly extracted from this plot. Note that: (i) relationship only assumes that all cells have same cortical rigidity K : it still holds for patterns displaying variable cell shapes, areas, and area elastic moduli X_i ; (ii) $p_i + p_j$ is expected to *increase* with relaxation velocity, unlike l_{ij} [Figure 2D and eq. (15)].

3.2) Data fitting and determination of side parameter values

We indeed found that $p_i + p_j$ increases with V_{ij}^o , as predicted by eq. (17) (Figure S2D-E): this constitutes an additional validation of the model, and prompted us to fit these experimental data to determine the model side parameters. For each dataset, determination of the line that best fits experimental data can provide characteristic time τ , mean zero-intercept $\langle \lambda \rangle$ and dispersion around this value σ_λ (Figure S2D-E). To best fit the available data, we used a procedure that integrates the information from quantitative analysis of side lengths (Figure 1F), and thereby takes advantage of the large statistics ($n \sim 5 \cdot 10^3$ sides for wt and *pten* cells) of our previous quantitative analysis that yielded the actual side length distribution for wt and *pten* tissues (Figure 1F).

In wt tissue, our quantitative analysis showed that the side length distribution is monomodal (Figure 1F). It displays a single peak at $\langle l \rangle^{WT} \approx 0.67$ with dispersion $\sigma_l^{WT} \approx 0.19$. To achieve wt data fit and parameter determination, we selected data points that were representative of wt side length distribution, namely the points for which side lengths lied in intervals centered around $\langle l \rangle^{WT}$, and being gradually widened from σ_l^{WT} to $4\sigma_l^{WT}$. For each set of selected data points, we plotted

$\frac{1}{2}(p_i + p_j)$ vs. v_{ij}^o , plotted the line best fitting these data, and determined the corresponding values of $\tau, \langle \lambda \rangle$ and σ_λ . We found that the line corresponding to the average of least squares along both axes was the most robust when varying the interval width from σ_l^{WT} to $4\sigma_l^{WT}$. Lastly, we averaged the parameter values over all interval widths. For the wt, we thus found a single value of side parameters $\langle \lambda_o \rangle = 2.28 \pm 0.25$, the standard deviation around this value $\sigma_{\lambda_o} = 0.35 \pm 0.10$, and the characteristic time $\tau = 37 \pm 7s$ (Figure S2D).

We applied the same procedure to fit *pten* tissue ablation data. In this case, the side length distribution is bimodal, displaying two peaks: one corresponds to long sides (L), the other one to short sides (S) (Figure 1F). We therefore applied the above procedure for each peak. The quantitative analysis of side length distribution yields $\langle l \rangle_L^{pten} \approx 0.81$; $\sigma_L^{pten} \approx 0.23$ and $\langle l \rangle_S^{pten} \approx 0.17$; $\sigma_S^{pten} \approx 0.09$. For the long side peak we found $\langle \lambda_L \rangle = 2.87 \pm 0.06$, the standard deviation around this value $\sigma_{\lambda_L} = 0.38 \pm 0.07$, and the characteristic time $\tau = 31 \pm 3s$ (Figure S2E). Before determination of parameter values corresponding to short sides, one should note that: (i) the characteristic time $\tau = 1/\mu K$ is not a *side specific* quantity (as opposed to side parameters λ), but a *cell specific* property, since it only depends on cell cortical rigidity K and cell coefficient μ : it has therefore been already determined; (ii) short sides ($l < 0.5$) were difficult to ablate: fewer experimental points representative of short sides were obtained. Thanks to (i), short sides were not used to determine the slope, but only to determine the corresponding zero-intercept $\langle \lambda_S \rangle$. Because of (ii), we extended the range of selected data points around the peak up to $6\sigma_S^{pten}$. We checked that, for all interval width, the selected “short side” data points did not overlapped with “long side” data points (one single overlapping point at width $6\sigma_S^{pten}$). We found $\langle \lambda_S \rangle = 1.81 \pm 0.06$ and $\sigma_S = 0.35 \pm 0.03$ (Figure S2E).

3.3) Conclusion

These results provide estimates of model parameters for both wt and *pten* tissues inferred from laser ablation experiments. Note that reachable values of side parameters, namely values lying in the interval $[\lambda - 2\sigma_\lambda; \lambda + 2\sigma_\lambda]$, all remain within the physical domain of our study $[0 \leq \lambda_k \leq p_H, \text{ eq. (7)}]$. Then, both side parameters values in *pten* cells surround the wt unique value: $\langle \lambda_S \rangle < \langle \lambda_o \rangle < \langle \lambda_L \rangle$, as if wt side parameter value λ_o has been “split” by the *pten* loss of function into the two values λ_S, λ_L .

4) Model predictions II: short side instabilities in *pten* tissue

After the determination of the experimental range of λ values in both wt and *pten* tissues, we determined the corresponding cellular patterns in our model.

4.1) Side parameter 2D diagram: short side instabilities

As a first step, we studied the possible cellular patterns obtained when parameters $(\lambda = \lambda_\alpha, \lambda_\epsilon)$ span the physical domain defined by eq. (7). Interestingly, only a limited region in the side parameter space allows simultaneous coexistence of the three types of sides, or equivalently, existence of six-sided cells (green region in Figure 2E). Within this stable domain all three sides can exist and have different lengths, all strictly positive ($l_k > 0$). At the domain boundary (green-gray interface), one side length is exactly zero. Outside this region, parameter values do not allow simultaneous coexistence of the three sides, and the side with lowest λ_k value (highest γ_k), i.e. the shortest one [eq. (14)] disappears before the energy minimum can be reached: this is the unstable domain (grey region in Figure 2E). Close to the transition value p_H , the slightest difference in λ_k values makes one side vanish.

In summary, our model predicts the existence of two regions in the side parameters space: (i) a stable domain where all three side types can coexist: hexagonal patterns are stable; (ii) an unstable domain, where the side with highest side parameter shrinks, become the shortest and vanishes (shortest side instability): hexagonal patterns are unstable.

4.2) wt and *pten* domains in the diagram

We now determine regions of the side parameter diagram corresponding to the experimental range of λ values in both *wt* and *pten* tissues. Without loss of generality, this determination can be restricted to $0 \leq \lambda_\epsilon \leq \lambda_\alpha = \lambda \leq p_H$, the other combinations being obtained by permutations of these parameters.

The side parameter range compatible with *wt* experimental measurements is the disk centered at (λ_o, λ_o) and of radius $2\sigma_\lambda$ (blue in Figure 2E). The *wt* parameter domain lies almost entirely within the stable domain, with its center on the honeycomb pattern line. This means that on average, *wt* tissues adopt a honeycomb pattern (Figure 2A, S2A), which can be distorted due to biological variability. A small proportion intersects the unstable domain, leading to few disappearing sides and rearrangements. This agrees with observations made in *wt* tissue (Figure 3A-C and Movie S2A).

For *pten* tissues, the experimental parameter domain is the ellipse centered at (λ_L, λ_S) and of axes $(2\sigma_{\lambda_L}, 2\sigma_{\lambda_S})$. The *pten* domain significantly differs from *wt*: it mainly lies outside the stable domain, and so does its center; however, a smaller but significant proportion intersects the stable domain. Consequently, most parameter values involve an unstable side that will shrink, become the shortest and disappear. Strikingly, the centroid of the stable part of *pten* domain corresponds to a cobblestone structure (Figure 2B, S2C) similar to observed patterns in *pten* tissue (Figure 1B).

4.3) Discussion: short side instability in *pten* tissue

We discuss here the consequences of short side instabilities in the tissue, i.e. when side parameters values belong to the unstable domain. For instance, if a side “ ε ” disappears (in red in inset of Figure 2A), because of fluctuations in acto-myosin contractility, and therefore of side lengths, occurring in the epithelium, a new side will appear right after. This new side either corresponds to the “old” one reappearing, or it involves two cells that were not in contact before, thus involving a rearrangement and a “new” side. Therefore, the new value $\lambda_\varepsilon^{new}$ associated to this new side can be very different from $\lambda_\varepsilon^{old}$, possibly leading to two scenarios: (i) either the new set of parameters ($\lambda = \lambda_\alpha, \lambda_\varepsilon^{new}$) now belongs to the stable domain: a new stable side is formed and remains ; (ii) or ($\lambda = \lambda_\alpha, \lambda_\varepsilon^{new}$) belongs to the unstable domain: the new side will shrink and disappear again.

This latter scenario is particularly relevant to *pten* side parameter values that mostly lie outside the stable domain. As mentioned in section 4.2, most parameter values thus involve an unstable side that will shrink, become the shortest, disappear, and possibly lead to formation of a new side that is also likely to remain in the unstable region, leading to a new rearrangement, and so on. In this scenario, short sides can therefore keep on rearranging several times. This short side instability could go on until a stable triplet is chosen and all three sides remain. Through this mechanism, parameter values ($\lambda = \lambda_\alpha, \lambda_\varepsilon$) could concentrate in the stable region over time.

Our results are consistent with experimental observations, and lead to new predictions. Indeed, given the parameter values determined from laser ablations, on average, the wt is expected to adopt a honeycomb-like structure involving very few cell rearrangements. Conversely, the *pten* tissue is expected to acquire an average structure in cobblestones, but, given the large unstable portion of its parameter domain, it is expected to undergo many more cell rearrangements (involving instability of cell shortest sides) as compared to wt. These predictions are confirmed by our experiments: most short sides in *pten* tissue are unstable, disappear and fluctuate (Figure 3D-F and Movie S2B) as opposed to wt tissue.

4 - Supplemental References

- Brand, A.H., and Perrimon, N. (1993). Targeted gene expression as a means of altering cell fates and generating dominant phenotypes. *Development* *118*, 401-415.
- Gemp, I.M., Carthew, R.W., and Hilgenfeldt, S. (2011). Cadherin-Dependent Cell Morphology in an Epithelium: Constructing a Quantitative Dynamical Model. *PLoS Comput Biol* *7*, e1002115.
- Glazier, J.A., and Graner, F. (1993). Simulation of the differential adhesion driven rearrangement of biological cells. *Phys Rev E Stat Phys Plasmas Fluids Relat Interdiscip Topics* *47*, 2128-2154.
- Goberdhan, D.C., Paricio, N., Goodman, E.C., Mlodzik, M., and Wilson, C. (1999). Drosophila tumor suppressor PTEN controls cell size and number by antagonizing the Chico/PI3-kinase signaling pathway. *Genes Dev* *13*, 3244-3258.
- Graner, F., Dollet, B., Raufaste, C., and Marmottant, P. (2008). Discrete rearranging disordered patterns, part I: robust statistical tools in two or three dimensions. *Eur Phys J E* *25*, 349-369.
- Holm, E.A., Glazier, J.A., Srolovitz, D.J., and Grest, G.S. (1991). Effects of lattice anisotropy and temperature on domain growth in the two-dimensional Potts model. *Phys Rev A* *43*, 2662-2668.
- Huang, J., Zhou, W., Dong, W., Watson, A.M., and Hong, Y. (2009). Directed, efficient, and versatile modifications of the Drosophila genome by genomic engineering. *Proc Natl Acad Sci U S A* *106*, 8284-8289.
- Kervrann, C., and Boulanger, J. (2006). Optimal spatial adaptation for patch-based image denoising. *IEEE Trans Image Process* *15*, 2866-2878.
- Landsberg, K.P., Farhadifar, R., Ranft, J., Umetsu, D., Widmann, T.J., Bittig, T., Said, A., Jülicher, F., and Dahmann, C. (2009). Increased Cell Bond Tension Governs Cell Sorting at the Drosophila Anteroposterior Compartment Boundary. *Current Biology* *19*, 1950-1955.
- Mao, Y., Tournier, A.L., Bates, P.A., Gale, J.E., Tapon, N., and Thompson, B.J. (2011). Planar polarization of the atypical myosin Dachs orients cell divisions in Drosophila. *Genes Dev* *25*, 131-136.
- Marée, A.F.M., Grieneisen, V.A., and Hogeweg, P. (2007). The Cellular Potts Model and Biophysical Properties of Cells, Tissues and Morphogenesis ; Single-Cell-Based Models in Biology and Medicine. In, A.R.A. Anderson, M.A.J. Chaplain, and K.A. Rejniak, eds. (Birkhäuser Basel), pp. 107-136.
- Marmottant, P., Raufaste, C., and Graner, F. (2008). Discrete rearranging disordered patterns, part II: 2D plasticity, elasticity and flow of a foam. *Eur Phys J E* *25*, 371-384.
- Mombach, J.C., Glazier, J.A., Raphael, R.C., and Zajac, M. (1995). Quantitative comparison between differential adhesion models and cell sorting in the presence and absence of fluctuations. *Phys Rev Lett* *75*, 2244-2247.
- Muller, H.A., and Wieschaus, E. (1996). armadillo, bazooka, and stardust are critical for early stages in formation of the zonula adherens and maintenance of the polarized blastoderm epithelium in Drosophila. *J Cell Biol* *134*, 149-163.
- Ouchi, N.B., Glazier, J.A., Rieu, J.-P., Upadhyaya, A., and Sawada, Y. (2003). Improving the realism of the cellular Potts model in simulations of biological cells. *Physica A: Statistical Mechanics and its Applications* *329*, 451-458.

Patel, P.H., Thapar, N., Guo, L., Martinez, M., Maris, J., Gau, C.L., Lengyel, J.A., and Tamanoi, F. (2003). *Drosophila* Rheb GTPase is required for cell cycle progression and cell growth. *J Cell Sci* 116, 3601-3610.

Wartlick, O., Mumcu, P., Kicheva, A., Bittig, T., Seum, C., Julicher, F., and Gonzalez-Gaitan, M. (2011). Dynamics of Dpp signaling and proliferation control. *Science* 331, 1154-1159.

Weinkove, D., Neufeld, T.P., Twardzik, T., Waterfield, M.D., and Leever, S.J. (1999). Regulation of imaginal disc cell size, cell number and organ size by *Drosophila* class I(A) phosphoinositide 3-kinase and its adaptor. *Curr Biol* 9, 1019-1029.